Applied Surface Science

An effective cascade strategy over a Sn-enriched phosphate material: upcycling a reductive adsorbent into an environmental catalyst

--Manuscript Draft--

Manuscript Number:	
Article Type:	Full Length Article
Keywords:	Environmental pollutants; Nitrogen oxides; Sustainability; Recycling; Reductive adsorption mechanism
Corresponding Author:	Sebastiano Campisi Università degli Studi di Milano Milano, ITALY
First Author:	Tiziana Avola
Order of Authors:	Tiziana Avola
	Sebastiano Campisi
	Marco Scavini
	Filippo Bossola
	Claudio Evangelisti
	Károly Lázár
	Antonella Gervasini
Abstract:	A calcium phosphate based material enriched with Sn (8.3 at.%, as revealed by X-ray photoelectron spectroscopy) was successfully used in the reductive adsorption of Cr(VI) to Cr(III) for water remediation and, after use, repurposed into a heterogeneous catalyst for the oxidation of NO into NO2. The use of multiple characterization techniques (Mössbauer spectroscopy, synchrotron X-ray diffraction, TEM, and HAADF-STEM/EDS) provided information on Sn-speciation, structural composition, and morphological features. Cassiterite (rutile-type SnO2) and hydroromarchite (tin oxide-hydroxide Sn6O4(OH)4) crystalline phases characterized the material, with also the presence of an amorphous Ca3(PO4)2 phase. Notably, about 15 mgCr(VI)•g-1 could be effectively reduced over a broad pH range, even in the simultaneous presence of various anions and cations, with concurrent adsorption of the resulting Cr(III), thanks to adsorption properties of the phosphate phase. The catalytic performances of the adsorbent after use in Cr(VI) reductive adsorption was studied at different temperatures (150-450 °C) and space velocities (15,000-80,000 h-1). About 90% of NO conversion at 350 °C was observed. This study highlights the adaptability and efficiency of the developed material across different environmental remediation processes.
Suggested Reviewers:	Georgeta Postole, PhD Catalysis and Environment Research Institute Lyon georgeta.postole@ircelyon.univ-lyon1.fr Expert in materials synthesis and characterization of surface/interface properties
	Antonio Aronne, PhD Full Professor, Universita degli Studi di Napoli Federico II anaronne@unina.it Expert in phosphate material synthesis and surface engineering
	Sergio Gustavo Marchetti, PhD Universidad Nacional de la Plata march@quimica.unlp.edu.ar Expert in Mossbauer spectroscopy

UNIVERSITÀ DEGLI STUDI DI MILANO
DIPARTIMENTO DI CHIMICA

DIPCHI
DIPARTIMENTO DI CHIMICA

To Professor H. Rudolph, PhD
Editor-in-Chief *Applied Surface Science*
Netherlands Defense Academy, Faculty of Military Sciences,
Breda, Netherlands

Dear Professor Rudolph,

We are pleased to submit our manuscript entitled: "*An effective cascade strategy at the Sn-enriched interface of a phosphate material: upcycling of an adsorbent into an oxidation catalyst*", by Tiziana Avola, Sebastiano Campisi, Marco Scavini, Filippo Bossola, Claudio Evangelisti, Károly Lázárd and Antonella Gervasini, for consideration for the publication in the journal of *Applied Surface Sciences*.

The presented research is the outcome of a collaborative effort that involved an international team of researchers from Università degli Studi di Milano, CNR-SCITEC Institute of Milano, CNR-ICCOM Institute of Pisa, and Centre for Energy Research, Nuclear Analysis and Radiography Department of Budapest, bringing together expertise from different backgrounds.

Our study builds on previous findings in the field of sustainable materials and provides new insights into the design and synthesis of sustainable materials with multifunctional interfaces for applications in environmental remediation and catalysis.
Specifically, in this manuscript, we present the synthesis and characterization of a sustainable tin-embedded calcium phosphate material. We demonstrated that the material is efficient in the reductive adsorption of hexavalent chromium and additionally it can be easily repurposed as a catalyst in an oxidation reaction for environmental and industrial catalysis importance (i.e., NO oxidation to NO_2). This dual functionality not only enhances the environmental sustainability of the material but also paves the way for the implementation of circular practices in environmental protection. Ultimately, our research goes beyond conventional materials for environmental remediation by incorporating multiple functionalities that enable upcycling with practical implications for addressing emerging environmental challenges.

The international collaboration enriched the study with a comprehensive characterization of composition, structure, morphology and surface reactivity of the material, by using several advanced physico-chemical techniques (synchrotron X-ray powder diffraction, Pair Distribution Function Analysis, TEM, HAADF-STEM/EDS, Mössbauer spectroscopy, temperature programmed reduction).

UNIVERSITÀ DEGLI STUDI DI MILANO
DIPARTIMENTO DI CHIMICA

We are confident that our work would meet the scope of *Applied Surface Science* and make a valuable contribution to the literature in the field.

All authors read and approved the final manuscript.

We look forward to the opportunity of sharing our research with the readers of *Applied Surface Science*.

Sincerely,

Sebastiano Campisi and Antonella Gervasini

Dipartimento di Chimica
Via Golgi, 19 – 20133 Milano (Italy) - Tel: +39.0250314261/254 www.chimica.unimi.it

Highlights

- Tin calcium phosphate as adsorbent and catalyst in environmental processes
- Sn^{2+} and phosphates ensured Cr(VI) reduction and Cr^{3+} adsorption up to 15 $mg \cdot g^{-1}$
- Upcycling of tin calcium phosphate adsorbent into an environmental catalyst

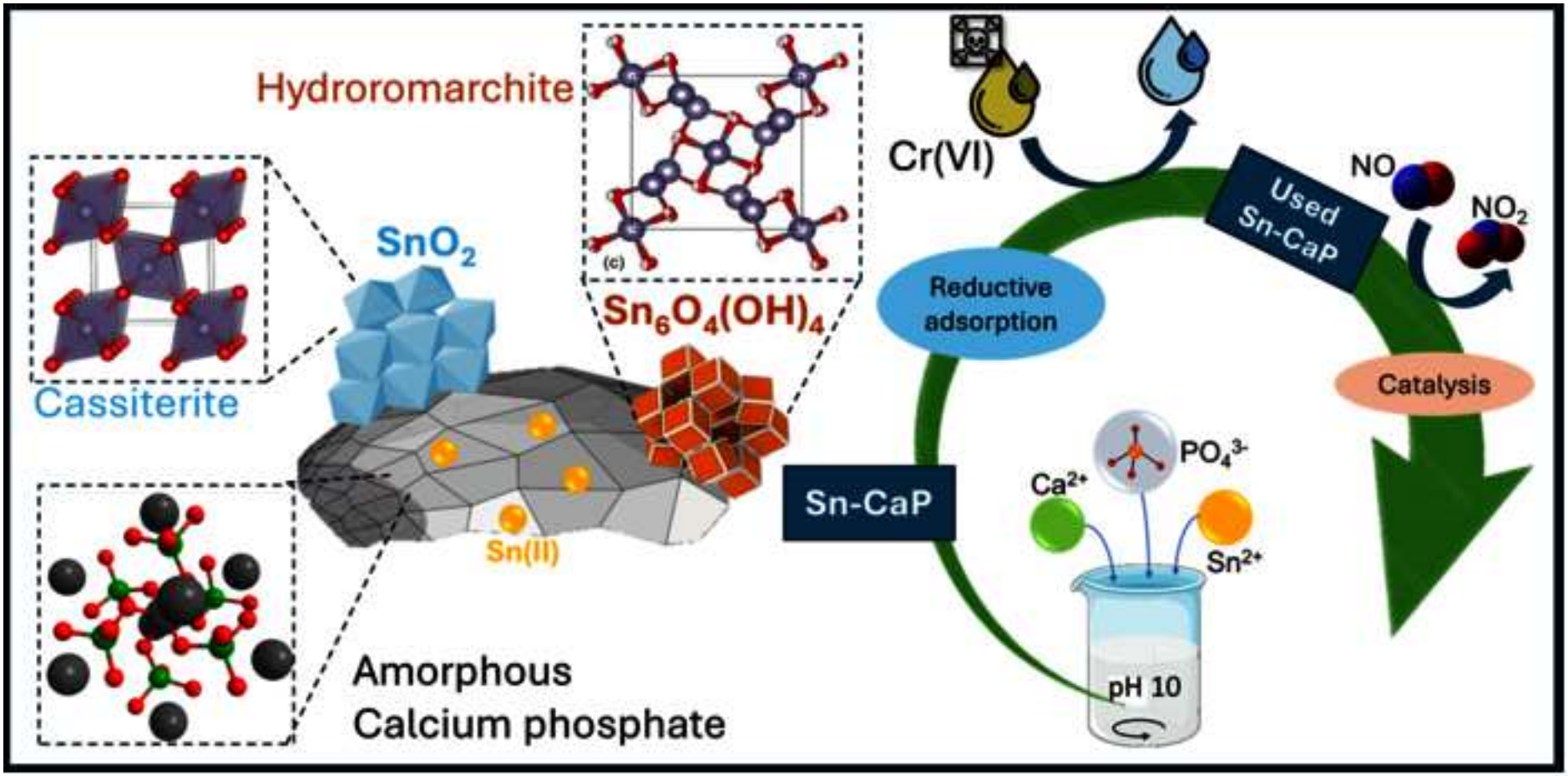

To *Applied Surface Science*

An effective cascade strategy over a Sn-enriched phosphate material: upcycling a reductive adsorbent into an environmental catalyst

Tiziana Avola,[a] Sebastiano Campisi,[a*] Marco Scavini,[a] Filippo Bossola,[b] Claudio Evangelisti,[c] Károly Lázár[d] and Antonella Gervasini[a*]

[a] Dipartimento di Chimica, Università degli Studi di Milano, via Camillo Golgi 19, Milano, 20133, Italy

[b] CNR - SCITEC - Consiglio Nazionale delle Ricerche, Istituto di Scienze e Tecnologie Chimiche "Giulio Natta", Via Camillo Golgi 19, Milano, 20133, Italy

[c] CNR - ICCOM - Consiglio Nazionale delle Ricerche, Istituto di Chimica dei Composti OrganoMetallici, Via G. Moruzzi 1, Pisa, I-56124, Italy

[d] Centre for Energy Research, Nuclear Analysis and Radiography Department, Institute for Energy Security and Environmental Safety, Konkoly-Thege M. Street 29-33, Budapest, H-1121, Hungary

* Corresponding authors:

sebastiano.campisi@unimi.it
antonella.gervasini@unimi.it

Abstract (200 words)

A calcium phosphate based material enriched with Sn (8.3 at.%, as revealed by X-ray photoelectron spectroscopy) was successfully used in the reductive adsorption of Cr(VI) to Cr(III) for water remediation and, after use, repurposed into a heterogeneous catalyst for the oxidation of NO into NO_2. The use of multiple characterization techniques (Mössbauer spectroscopy, synchrotron X-ray diffraction, TEM, and HAADF-STEM/EDS) provided information on Sn-speciation, structural composition, and morphological features. Cassiterite (rutile-type SnO_2) and hydroromarchite (tin oxide-hydroxide $Sn_6O_4(OH)_4$) crystalline phases characterized the material, with also the presence of an amorphous $Ca_3(PO_4)_2$ phase.

Notably, about 15 $mg_{Cr(VI)}.g^{-1}$ could be effectively reduced over a broad pH range, even in the simultaneous presence of various anions and cations, with concurrent adsorption of the resulting Cr(III), thanks to adsorption properties of the phosphate phase. The catalytic performances of the adsorbent after use in Cr(VI) reductive adsorption was studied at different temperatures (150-450 °C) and space velocities (15,000-80,000 h^{-1}). About 90% of NO conversion at 350 °C was observed.

This study highlights the adaptability and efficiency of the developed material across different environmental remediation processes.

Keywords

Environmental pollutants; Nitrogen oxides; Sustainability; Recycling; Reductive adsorption mechanism

1. Introduction

In recent years, there has been a remarkable increase in interest regarding the development of innovative functional and multifunctional materials, tailored for a wide range of diverse applications across various fields, including but not limited to electronics, nanomedicine, environmental sciences, and numerous other fields [1–7]. Beyond mere functionality, a pivotal aspect is linked to the lifecycle of each material, encompassing how it is sourced, utilized, and ultimately disposed of. Attention to sustainability and criteria of circular economy must be even more emphasized when developing materials for environmental remediation (air and waters protection) [8–12].

Over the last years, metal phosphates have emerged as a prominent category of sustainable phosphorus compounds [13]. The success of these materials stems from their structural variety, driven by the diverse arrangements of phosphate anions, their capacity to coordinate with numerous cations, and the ability to incorporate additional anions or molecules. These factors collectively contribute to the creation of a wide range of materials characterized by high versatility and functionality. Metal phosphate have been successfully proposed as electrodes for energy storage [14], as optical materials [15,16], as adsorbents [17–20], and as catalysts [21–28]. Considering the abundance of natural phosphate reservoirs, alongside the potential sourcing from waste materials and enhanced bioavailability, phosphate-based materials emerge in environmental preservation field as a promising alternative from both an economic standpoint and in terms of sustainability, as discussed earlier.

An interesting waste derived source of phosphates is associated with leachates from dissolution of ashes of vegetable biomass incineration that are rich in calcium and phosphates.

In addition, the multifunctional character of phosphate materials opens to the possibility to reusing or upcycling thus adhering to circular economy principles. Recently, Campisi *et al.* [29] developed an "adsorbent-to-catalyst" strategy to handle a used adsorbent material based on hydroxyapatite, a crystalline calcium phosphate material. Specifically, tin-enriched hydroxyapatite was proven to be highly effective in the Cr(VI) reductive adsorption process, able to remove up to 20 mg_{Cr} g^{-1}. The used material was successfully upcycled into catalyst in the selective catalytic oxidation (SCO) of NH_3 and CH_4.

Drawing inspiration from the promising performance observed in tin-enriched hydroxyapatite, this study delves into the potential of synergistically merging two core advantages of phosphate materials, namely their possible extraction from wastes and their upcycling into catalysts after use as adsorbents. To achieve this, we prepared a tin-enriched phosphate material through a one-pot co-precipitation method, which mimics the precipitation of value-added material from phosphate tailings [30].

The prepared material was characterized in its morphological and structural properties by X-ray powder diffraction (XRPD), N_2 adsorption/desorption analyses. Electron microscopy (TEM and

HAADF-STEM/EDS) was applied to verify the distribution of tin at the surface. In addition, Mössbauer spectroscopy was used to investigate tin speciation in the samples after synthesis and after long time exposure to atmosphere, to study the kinetics of the Sn(II) oxidation to Sn(IV).

Performance in the Cr(VI) reductive adsorption was evaluated in a wide range of pH (2-11), even in the simultaneous presence of various anions and cations. Further, a kinetic study over about ten months tracked the oxidative aging process of Sn(II) to Sn(IV), resulting in a gradual decline in its reducing activity, as expected. Then, a regeneration procedure was developed to restore the pristine activity of air-aged Sn-CaP.

Finally, in a circular economy context, selected samples used in the Cr(VI) removal were then upcycled into catalysts with success in an important environmental reaction, specifically the oxidation of NO to NO_2.

2. Materials and methods

2.1. Materials

Calcium nitrate tetrahydrate, ($Ca(NO_3)_2 \cdot 4H_2O$, >99.0%, ACS), iron(III) nitrate nonahydrate ($Fe(NO_3)_3 \cdot 9H_2O$, ACS), tin chloride dihydrate ($SnCl_2 \cdot 2H_2O$, ≥98.0% oxidimetric assay) and potassium bichromate ($K_2Cr_2O_7$, ≥99.0% oxidimetric assay) were purchased from Carlo Erba. Diammonium hydrogen phosphate ($(NH_4)_2HPO_4$, >98.0%), sodium nitrate ($NaNO_3$, ≥99.0%, ACS Reagent), sodium sulfate decahydrate ($Na_2SO_4 \cdot 10H_2O$, ≥99.0%, ACS Reagent), cobalt nitrate hexahydrate ($Co(NO_3)_2 \cdot 6H_2O$, 98%) and nickel nitrate hexahydrate ($Ni(NO_3)_2 \cdot 6H_2O$, ≥98.5%) salts were from Sigma-Aldrich. Sodium chloride (NaCl, ≥99.5%) and magnesium nitrate hexahydrate ($Mg(NO_3)_2 \cdot 6H_2O$, ≥99%) were purchased from Merck. Hydrochloric acid (37 wt%, Merck) and ammonium hydroxide solution, NH_4OH (28-30 wt%, Fluka) were used for pH adjustment. Hydrazine solution (98%) was from Carlo Erba. Nitrogen, 99.9995% purity from SAPIO was used as inert gas. All the solutions were prepared with MilliQ water ($\rho \geq 17.5$ MΩ cm; TOC, 2 ppb).

2.2. Synthesis and regeneration of tin-containing calcium phosphate

2.2.1. Synthesis of Sn-CaP

Tin-containing calcium phosphate (Sn-CaP) was prepared by one-pot co-precipitation method (Scheme 1), taking inspiration from a published laboratory report of Duncan *et al.* [31] with some modifications. Aqueous solutions of $Ca(NO_3)_2$ 0.173 M, $(NH_4)_2HPO_4$ 0.140 M and $SnCl_2$ 0.080 M were used as precursors for the synthesis of Sn-CaP in order to obtain a Sn nominal concentration of 35 wt. % and a (Ca + Sn)/P molar ratio of 1.80 (product yield, 94%). All the three precursor solutions were added simultaneously at a flow rate of 1.7 mL/min to a *3-neck* flask containing an NH_4OH

solution at pH 10. The system was kept in a water bath thermostated at 32 °C and maintained under nitrogen atmosphere and stirring until then all three solutions were quantitatively transferred. During the synthesis, the pH was maintained at 10 by periodic addition of a small amount of a 28-30% NH_4OH solution. During the first half hour, some flocculation was observed with simultaneous light blue coloration of the suspension (Scheme 1); then, a white solid precipitate was formed. Finally, the resulting solid was filtered through a Büchner funnel, washed with water, and dried under vacuum at 50 °C overnight.

Typically, the samples were kept in closed vessel under air atmosphere. Then, some selected samples batches were stored under nitrogen atmosphere.

Other calcium phosphate samples with different Sn content (from 20 wt.% to 45 wt.%) were synthesized with the same preparation protocol for comparative studies.

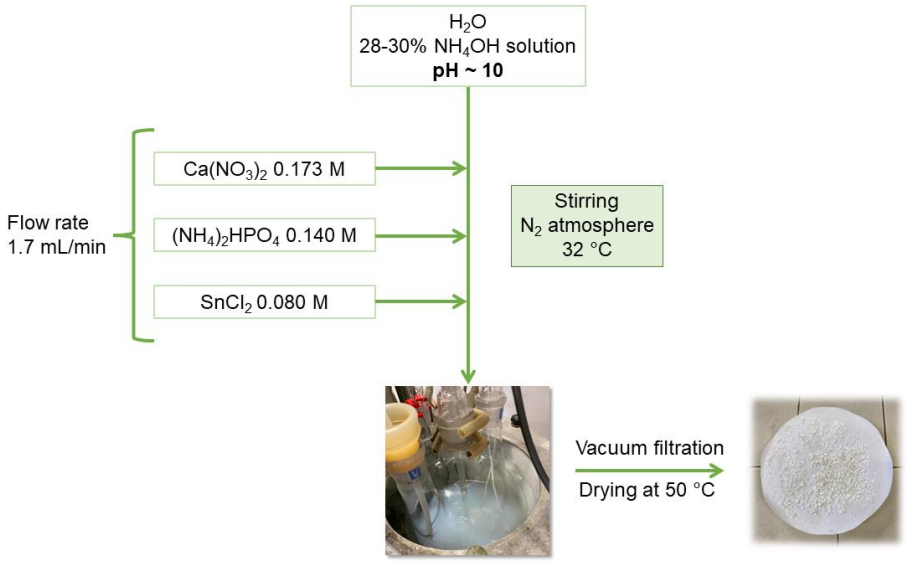

Scheme 1. Schematic representation of the *one-pot co-precipitation* synthesis of Sn-CaP samples.

2.2.2. Regeneration of air-aged Sn-CaP

Air-aged Sn-CaP sample was treated in a quartz cylindrical tube with 5-8 vol.% flowing H_2/Ar gas (20 ml min^{-1}) for 1-4 h at 350 °C, followed by cooling down to room temperature in Ar flow (20 ml min^{-1}) and left overnight in static slight overpressure of Ar.

2.3. Characterization of material

2.3.1. Determination of point of zero charge (PZC)

Point of zero charge (PZC) value was determined by salt addition method. Ca. 0.1 g of Sn-CaP sample was placed in six flasks cointaining 5 mL of KCl solution (0.1-0.5 M) at adjusted pH values (5-10). All the flasks were kept in a water bath thermostated at 25 °C and under magnetic stirring for 24 h.

Final pH values were measured, and the variation between initial and final pH values was calculated and plotted against initial pH values. The PZC corresponds to the intercept with the x-axis.

2.3.2. Determination of elemental composition

The Sn loading of Sn-CaP samples was quantified by Inductively Coupled Plasma Mass Spectrometry (ICP-MS) using an iCAP Q ICP-MS (Thermo Fischer Scientific) configured with an ASX-560 Autosampler. Solids were digested with 3 mL HCl 37 % and 1 mL HNO_3 at 110 °C for two hours prior to analysis.

Elemental composition of selected samples was evaluated using Prompt-gamma activation analysis (PGAA). In particular, the presence of elements like H, O, P, Cl, Ca, Sn, was quantified. Principles of PGAA method and the upgraded equipment are described in previous works [32,33]. The sensitivity in determination of elements varies within several order of magnitudes, for chlorine is particularly high, or, in reverse, low for oxygen [32]. The samples were measured with a neutron flux of 10^8 n cm^{-2} at nominal temperature of neutrons of -133 °C. The γ-radiation profiles were evaluated with a Windows based Hyperlabs software [34].

2.3.3. X-ray photoelectron spectroscopy (XPS)

A KRATOS AXIS ULTRA DLD spectrometer (Kratos Analytical) equipped with a magnetic immersion lens, a hemispherical analyzer, and a delay line detector was used to collect XPS spectra. Initially, a survey spectrum of the sample was collected in the electron binding energy range of 0-1100 eV. Then, a high-resolution spectrum, with a focus on the Cr 2p line of selected sample, was acquired within the interval of 570-605 eV. The band of adventitious carbon (C1s, at 284.6 eV) was ruled out in the quantitative determination of the surface species.

2.3.4. ^{119}Sn Mössbauer spectroscopy

^{119}Sn Mössbauer spectra were recorded with a KFKI spectrometer using a 0.56 GBq $Ca^{119}SnO_3$ source with constant acceleration mode. The δ isomer shift values are calibrated against a spectrum of a combined SnO_2 and β-Sn absorber at room temperature. Samples were measured at -193 °C and at room temperature (27 °C). Spectra were evaluated by least-square fitting with superpositions of Lorentzian shape lines using the SIRIUS code [35].

2.3.5. X-ray powder diffraction (XRPD)

X-Ray powder diffraction (XRPD) patterns were collected using a PANanalytical XPert PRO powder diffractometer operating with an X-ray source at 40 kV and 25 mA in the range between 5°-60° (2θ), step of 0.02° in 2θ and collection time of 50 s.

Synchrotron radiation powder diffraction data have been collected at the ID15A beamline of the ESRF [36], using E=94.999 keV (that corresponds to λ=0.130510 Å).

The sample was placed in Kapton© capillary with a diameter of 1 mm and measured at room temperature. Diffracted photons were detected using *Dectris Pilatus3 X 2M* utilising a *CdTe* sensor.

Several frames were collected at two sample-detector distances: the closest one (334.2 mm) was adopted to maximize the Q (=4πsinθ/λ) interval for Pair Distribution Function Analysis; the longer one (1034.6 mm) was selected to optimize the Q space resolution for reciprocal space analysis purposes.

Wavelength, sample-detector distance, and azimuthal integration parameters were calibrated on the Cr_2O_3 reference. The detector mask was created with the program FIT2D [37]; calibration and azimuthal integration were all performed using the program pyFAI [38]. Details about data analysis are reported in paragraph S.1 of ESI.

2.3.6. N_2 adsorption-desorption isotherms at -196 °C

Specific surface area and porosity were evaluated by collecting N_2 adsorption-desorption isotherms at the liquid nitrogen temperature with a Sorptomatic 1990 version instrument (Thermo Scientific). Prior to the analysis, the dried sample was outgassed for 16 h at 150 °C under high vacuum conditions to remove moisture from all pores. MILES-200 program and MILEADP software were used for data elaboration. The low-pressure region of the adsorption isotherm has been modelled using the 3-parameter BET equation, while the desorption isotherm has been analyzed using the B.J.H. (Barrett-Joyner-Halenda) model within the range of $0.3<p/p^0<0.95$. These models were employed to determine the specific surface area and pore volume distribution, respectively.

2.3.7. Transmission electron microscopy energy-dispersive X-ray spectroscopy (S/TEM-EDS)

Morphological and structural characterization by Transmission Electron Microscopy (TEM) was performed using a Talos™ F200X G2 TEM microscope (Thermo Scientific). Energy dispersive X-ray spectra (EDS) and element maps were collected along with HAADF-STEM (high angular annular dark field scanning transmission electron microscopy) micrographs and four-detector SuperX Energy Dispersive. Samples for analysis were prepared by their suspension in *iso*-propyl alcohol and ultrasonically dispersed followed by a deposition of a drop of the suspension on a holey carbon copper grid (300 mesh).

2.3.8. Temperature programmed reduction (H_2-TPR)

Temperature programmed reduction (TPR) experiments using H_2 were performed in a PulseChemisorb 2700 (Micromeritics) instrument. Tipically, TPR measurements were carried out on ca. 40 mg of the fresh and aged samples by raising the temperature from room temperature to 800 °C at a rate of 10 °C min^{-1} in 8 vol.% flowing H_2/Ar gas (20 ml min^{-1}). Sample pre-treatment was done at 130 °C for 30 minutes under Ar flow (20 mL min^{-1}) prior to the analyses. The consumption of hydrogen was monitored with a thermal conductivity detector (TCD).

2.4. Hexavalent chromium reductive adsorption tests

Fresh and aged Sn-CaP samples were tested for reductive adsorption of Cr(VI) in batch experiments. The test was carried out at 25.0 ± 0.5 °C, following the same procedure described in a previous work [39], using an initial Cr(VI) concentration of 100 mg L^{-1} and exploring a range of pH values from 2 to 11. The residual concentration of Cr(VI) was determined by UV-vis spectrophotometric analysis working at 540 nm by using 1,5-diphenyl carbazide (DPC) method [40].

The total chromium concentration was determined by Inductively Coupled Plasma Mass Spectrometry (ICP-MS, *UNI EN ISO 17294-2 method*). The monitoring of both Cr(VI) and total chromium concentrations allowed for the assessment of removal efficiency (η, %) and removal capacity (q_e, $mmol_{Cr}$ g^{-1}) (see paragraph S.2 of ESI for equations).

Kinetic study of the reductive adsorption of Cr(VI) was evaluated performing multiple tests at 25 °C in independent batch reactors containing an aqueous solution of Cr(VI) 50 mg L^{-1} at generated pH of ~5.65 (dosage of 4.5 g L^{-1}). The effect of co-presence of selected cations (i.e., Fe, Co, Ni, Ca and Mg) and anions (chloride, nitrate, sulphate) on the reductive adsorption kinetics was investigated and the initial concentration of each ion is reported in Table S.1 [41]. The reaction was stopped after 3, 10, 50, 120, 180, 240 min by filtration and separation of Sn-CaP powder from each reactor to collect kinetic profiles as a function of time.

All the collected experimental data were fitted using different kinetic models, i.e., the pseudo-first order (PFO), pseudo-second order (PSO) and Elovich models. A detailed description of the models and statistical parameters used is reported in paragraph S.2 of ESI.

2.5. Catalytic tests

Catalytic tests of NO oxidation to NO_2 were performed in a continuous reaction line as described in a previous work [42] with an online FT-IR spectrometer (Bio-Rad FTS 3000 Excalibur Series, resolution 2 cm^{-1}) for the determination of the fed and vented gaseous species. The catalytic behaviour of selected samples, namely, fresh and used Sn-CaP was evaluated in the NO selective catalytic

oxidation (NO-SCO) to NO_2. Before testing, samples were calcined in air at 550 °C for 1 h (heating rate of 1 °C min^{-1}).

Prior to the catalytic tests, a given amount of the so-prepared catalyst (ca. 0.12 g) underwent to thermal pre-treatment at 118 °C for 30 min under O_2/N_2 flow (20% v/v) at 6 NL h^{-1}. The catalytic tests were carried out with a fed gaseous mixture consisting of 800 ppm NO, 40,000 ppm O_2 and N_2 to balance (O_2/NO = 50). NO oxidation was studied as a function of temperature, ranging from 150 °C to 450 °C, keeping the gas hourly space velocity (GHSV) constant at 50,000 h^{-1}. Then, at selected temperature of 350 °C, the effect of GHSV on sample activity was investigated in the range of 15,000 - 80,000 h^{-1} by varying the total flow rate from 2 NL h^{-1} to 9 NL h^{-1}.

The total absorbance of all the IR active species (NO and NO_2) was continuously recorded as a function of time/temperature and their concentration was determined by the intensity of typical absorbance lines (1875 cm^{-1} and 1626 cm^{-1} for NO and NO_2, respectively), once known the molar extinction coefficient of each species.

3. Results and discussion

3.1. Sn-CaP synthesis

A calcium phosphate material enriched with Sn (Sn-CaP) was prepared by a one-pot co-precipitation method as described in the experimental section (Scheme 1). The Sn-CaP sample under investigation has been chosen from a range of similar prepared samples, each one at varying Sn content, spanning from 20% to 45% by weight. Specifically, the Sn-CaP sample in focus has been crafted with a nominal Sn content of 35% by weight. Remarkably, it exhibited an approximate tin surface concentration of 8 at.% (as discussed later), a value closely aligned with the optimal tin surface concentration observed in the Sn-hydroxyapatite material, which demonstrated the best performance in the reductive adsorption of Cr(VI) [29].

In meeting sustainability criteria, we utilized simple and cost-effective salts such as $SnCl_2$, $Ca(NO_3)_2$, $(NH_4)_2HPO_4$ as precursors for tin, calcium, and phosphate. The employed one-pot precipitation method allowed the quantitative incorporation of Sn, Ca, and P into the final precipitate, Sn-CaP, as confirmed by ICP-MS analysis, with only negligible amounts of the three elements detected in the washing waters.

Furthermore, our synthesis method offered distinct advantages over the preparation route of Sn-functionalized hydroxyapatite material [29], which shares the same main components of tin, calcium, and phosphate. The latter material is typically prepared through a two-step synthetic process involving post-synthesis functionalization. Initially, calcium hydroxyapatite was synthesized via co-precipitation, followed by the addition of tin through a wet deposition method.

From this perspective, the one-pot procedure employed in the synthesis of Sn-CaP offers a simplified approach, reducing the number of synthetic steps required and thereby minimizing waste production and energy consumption.

The bulk and surface composition of Sn-CaP was determined by ICP-MS, PGAA, XPS and EDS analyses and results are summarized in Table 1. Both bulk techniques, such as ICP-MS and PGAA, are in excellent agreement to evaluate the chemical composition of Sn-CaP sample as shown in Table 1. Concerning Sn, a lower experimental wt.% was obtained compared to the nominal one (expected Sn content of 35 wt.%), likely due to the inclusion of high amount of water, as indicated by hydrogen content as determined by PGAA. Only a negligible extent of chlorine, derived from the $SnCl_2$ precursor, was revealed by PGAA analysis, meaning that tin species might be incorporated in Sn-CaP as oxo/hydroxy tin complexes. In addition, the absence of chlorine let us to rule out the possible formation of any chloride phosphate phases, such as chloro-apatites [43].

Surface chemical composition of Sn-CaP was determined performing XPS analysis and the acquired survey spectrum of Sn-CaP sample was shown in Fig. S.1. The presence of the typical peaks attributed to O 1s (530.9 eV), Sn 3d (486.5 eV), Ca 2p (347 eV) and P 2p (132.9 eV) confirms the presence of these elements at the surface of the synthesized sample. The surface (Ca + Sn)/P molar ratio was 1.77, which reflected the bulk value, as determined by considering the molar concentration of used precursors (Scheme 1); this confirmed a good compositional homogeneity of the sample from bulk to surface layers. The surface elemental composition of Sn-CaP was also assessed by EDS and the obtained results are also gathered in Table 1. The quantification of Sn (8.6 at. %) was consistent with that determined by XPS analysis.

Table 1. Composition of Sn-CaP sample obtained from different techniques.

Element	**Ca**	**Sn**	**P**	**O**	**Cl**
ICP (wt. %)[a]	23.3	25.6	8.3	n.d.	n.d.
PGAA (wt. %)[b,c]	18.0	27.0	11.0	43.0	0.11
XPS (at. %)	15.3	8.3	13.3	63.1	n.d.
EDS (at. %)	17.7	8.6	12.5	60.9	0.3

[a] obtained after solid digestion

[b] relative error in determination of components is ca. 8 %

[c] hydrogen concentration detected: 33.8 at.% corresponding to 1.92 wt.%

3.2. Sn-CaP structure

The structure of Sn-CaP was determined by XRPD analysis, which revealed complex and poorly defined patterns indicating the co-presence of crystalline and amorphous phases in Sn-CaP sample

(Fig. S.2). The pattern was dominated by some intense reflections ascribable to the SnO_2 cassiterite phase, while the presence of other less intense peaks and broad bumps required further investigation. An in-depth study of amorphous and crystalline phases was then conducted through XRPD analyses using synchrotron radiation. Fig. 1 reports the experimental pattern of Sn-CaP after subtracting the Kapton© capillary (black symbols). The experimental curve exhibits both sharp Bragg peaks and broad bumps, as indicated by the green curve, suggesting the presence of both crystalline and amorphous phases.

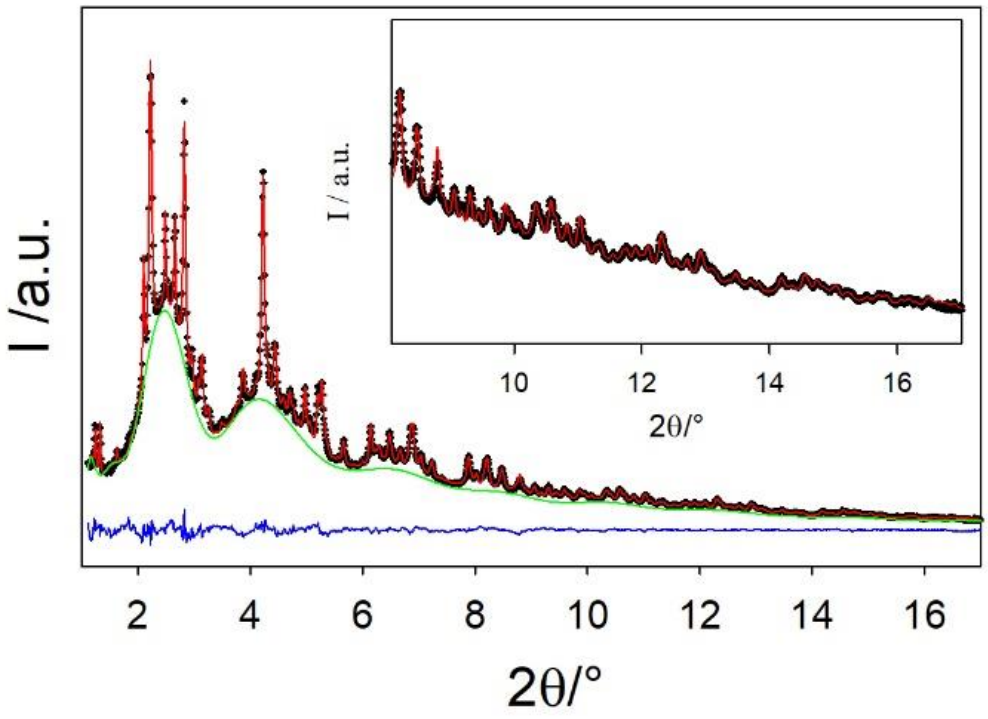

Figure 1. Experimental pattern of Sn-CaP after subtraction of the Kapton capillary (black symbols), best Rietveld refinement (red curve), calculated background (green curve) and difference curve (blue curve). The inset highlights the high 2θ range of the XRPD pattern.

Two crystalline tetragonal phases were identified: cassiterite, the Rutile-type SnO_2 (space group $P4_2/mnm$ [44]), and hydroromarchite, tin oxide-hydroxide $Sn_6O_4(OH)_4$ (space group $P4/mnc$ [45,46]), the former containing Sn(IV) and the latter exclusively Sn(II), respectively. Refer to paragraph S.3 of ESI for a brief in-depth analysis of the latter phase.

The best Rietveld refinement is depicted in Fig. 1 as a red curve, accompanied by the calculated "background" (green curve) and the difference curve (blue curve), while the fitted parameters are presented in Table S.3 of the ESI. According to the refinement, the weight fractions of the SnO_2 and $Sn_6O_4(OH)_4$ phases are ≈66% and ≈34%, respectively. However, these phase fractions cannot be considered representative of the entire sample composition. As indicated by the shape of the green (background) curve of Fig. 1, some amorphous phase should be present; the nature and concentration

of which cannot be determined by Rietveld refinement, which only considers the Bragg peaks. Therefore, as specified in the experimental section, XRPD data were collected over a wide Q range, and after suitable corrections/normalizations, the structural function S(Q) contributed by both Bragg peaks and diffuse scattering was obtained. Subsequently, the S(Q) was Fourier transformed to compute the pair distribution function PDF/G(*r*) of the Sn-CaP sample, depicted as a black curve in panel A of Fig. 2 over a wide *r*-range.

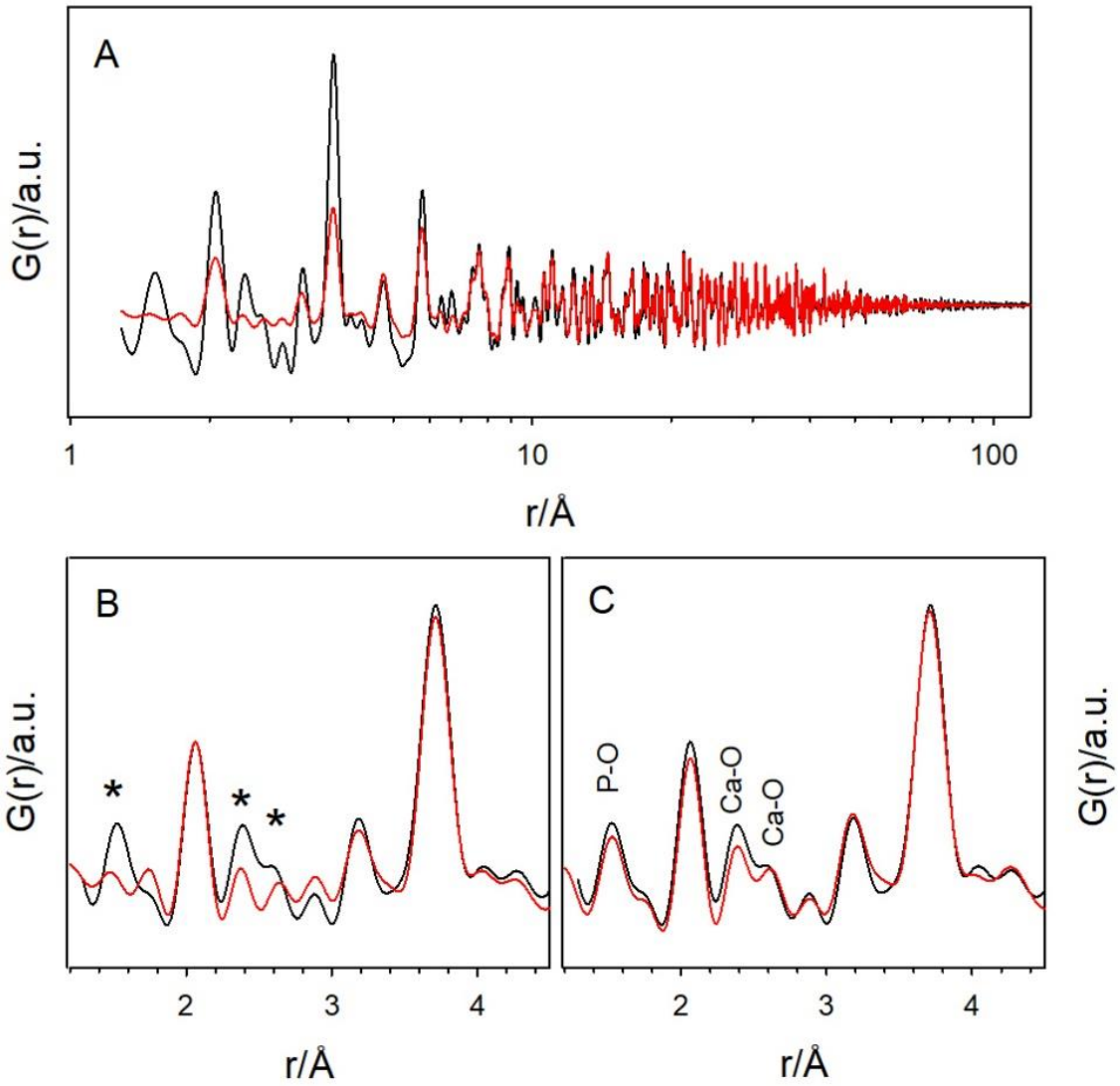

Figure 2. X-ray total scattering derived pair distribution function (PDF) in real space. Experimental G(r) function and the computed one are shown as black and red curves, respectively. The r-scale is logarithmic in panel A and linear in panels B and C. The computed G(r) functions in A, B, C panels derive from different structural models. See text for details.

Initially, the G(*r*) was analysed using the RSRA (Real Space Rietveld Analysis) across the entire *r*-range, applying the same SnO_2 and $Sn_6O_4(OH)_4$ models as in the Rietveld analysis. However, as it will be shown below, several experimental peaks at short range were significantly underestimated or

even absent in the model curve. Indeed, the G(r) function also includes structural information of the possible amorphous phase(s), characterized by very short spatial coherence lengths. Consequently, the following refinement strategy was adopted: first, the G(r) was fitted in the 12-120 Å range, allowing the cell parameters, positional degree of freedom, two thermal parameters for Sn and O respectively, and the volume averaged particle diameters D_V of the SnO_2 (D_V ≈11 nm) and $Sn_6O_4(OH)_4$ (D_V ≈12 nm) phases to vary. The lower limit of the r-range was selected after several tests to avoid deviations from the average structure at low r.

Then, the model was extended to the lowest r values, with all parameters fixed. The fitted curve is depicted as a red curve in Fig. 2A. The logarithmic scale of the r axis highlights the discrepancies between the fit and the experimental data at low r values: the intensities of the G(r) peaks at r ≈2.06 Å, ≈3.18 Å, ≈3.72 Å, ≈5.71 Å are significantly underestimated, while others at r ≈1.50 Å, ≈2.37 Å, ≈2.61 Å are even absent in the model.

In a third step, focus was placed on the very short range (1.2-4.5 Å), allowing only the cell constants and the phase fractions of the two phases to vary. Increasing the scale factors of both phases improved the agreement between the experimental and calculated peak intensities of the "underestimated" peaks, as shown in panel B of Fig. 2. This anomalous behaviour may tentatively be rationalized by assuming that a fraction of the particles has a very small coherence length; however, the peaks labeled by asterisks are still absent in the model.

Since elemental analysis of Sn-CaP indicated the presence of a large amount of calcium and phosphorus, different calcium phosphate phases were considered; among them, the rhombohedral β-$Ca_3(PO_4)_2$ form [47] supplied the best fit. Fig. 2C displays the computed G(r) curve in red, while Ca-O and P-O labels indicate the atoms of the calcium phosphate phase involved in each G(r) peak, which was not indexed in the previous refinement approaches.

Based on the computed phase fractions (PDF), the Ca/Sn atomic ratio is approximately 2.8, slightly higher than the Ca/Sn≈2 ratio revealed by PGAA measurements. However, this last PDF result must be considered semi-quantitative because a periodic structural model is applied to an amorphous phase. In addition, it is not possible to exclude partial Ca(II)/Sn(II) ion substitution in the amorphous phosphate, which would decrease the Ca/Sn ratio.

Finally, attempts to extend the last structural model to larger r-range were unsuccessful due to the very short crystallographic coherence of the calcium phosphate phase, confirming its amorphous nature.

3.3. Sn-CaP morphology and microstructure

The morphological and microstructural properties of Sn-CaP were investigated by collecting N_2 adsorption/desorption isotherms at -196 °C and performing TEM and HAADF-STEM/EDS analyses. The collected N_2 adsorption/desorption isotherm is shown in Fig. 3 and indicates a solid porous material, where the presence of two families of mesopores with a slight contribution of microporosity can be identified. A certain level of microporosity is evident in the low-pressure region ($p/p^0<0.1$) of the isotherm, while a clear hysteresis is observed at $0.4<p/p^0<0.85$, which is typical of mesoporosity presence. According to the IUPAC classification, the hysteresis loop in the desorption branch appears to fit both type H4 and type H5 hysteresis, reflecting the complexity of the porous network in relation to the structural complexity of the material, as evidenced by XRPD results.

Surface area and porosity were determined using the 3-parameters BET model to fit the low-pressure region of the adsorption branch and B.J.H. model, respectively. A specific surface area of 60 $m^2\ g^{-1}$ was determined (Table S.2). The mesopore size distribution, shown in the inset of Fig. 3, indicates two main populations of pore size. The primary family is centered at approximately 4 nm, while other pores fall within the diameter range of 5-7 nm.

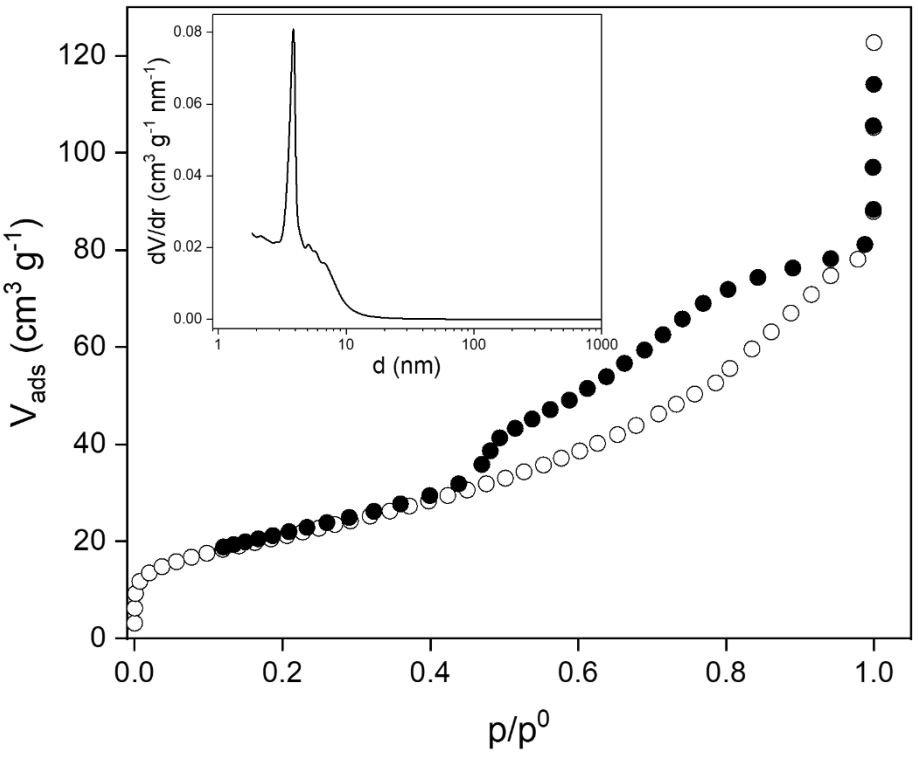

Figure 3. N_2 adsorption/desorption isotherms on Sn-CaP sample and pore volume distribution (calculated with B.J.H. model) in the inset.

TEM and HAADF-STEM micrographs of the Sn-CaP sample are presented in Fig. 4. TEM analysis of the Sn-CaP sample revealed the presence of small nanocrystalline domains highly dispersed on the material grains, which are mainly present in a quite narrow size distribution (ranging from 5 to 20 nm) (Fig. 4). Interestingly, this result is consistent with the PDF findings, which evidenced the presence of SnO_2 and $Sn_6O_4(OH)_4$ phases with a volume averaged particle diameter (D_v) of ca. 11-12 nm, falling within the same size range. The presence of SnO_2 particles was further confirmed by the TEM image acquired in high-resolution mode shown in Fig. 4B. Lattice planes extend along the particles without any stacking faults or twins, indicating their single crystalline nature. Lattice fringe analysis exhibited spots in the Fourier Transform (FT) pattern at 3.3 Å, which are attributed to the spacing of (1 1 0) planes of the tetragonal SnO_2 phase [JCPDS of 41-1445], consistent with the XRPD results.

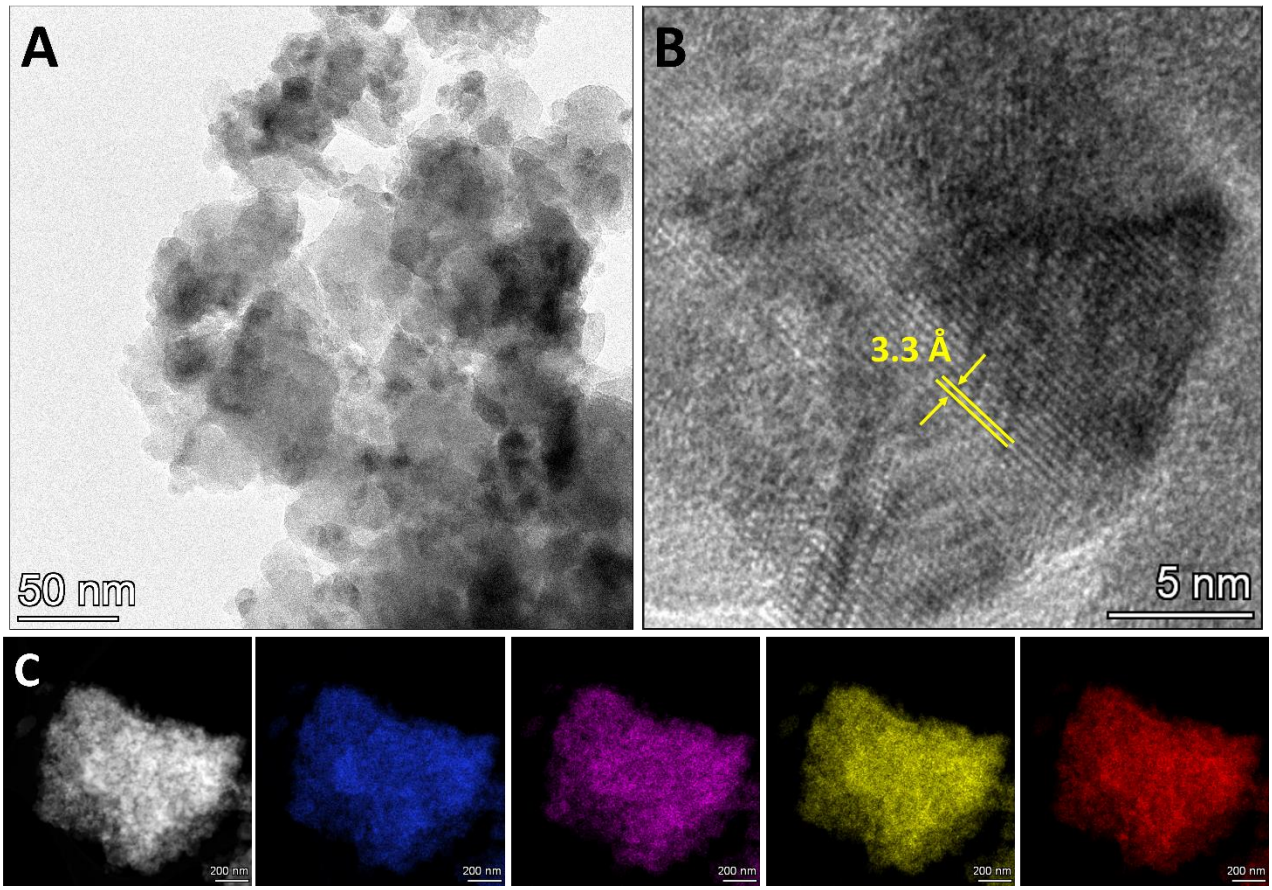

Figure 4. Morphological and structural characterization of Sn-CaP: representative TEM micrograph of Sn-CaP (A) and HRTEM image of a SnO_2 nanocrystalline domain (B); bottom: HAADF-STEM reference micrograph of a representative grain of Sn-CaP and the corresponding EDS element mapping of oxygen (blue), phosphorous (violet), calcium (yellow) and tin (red).

HAADF-STEM/EDS analysis of Sn-CaP (Fig. 4, C panel) showed a very high dispersion of Sn onto the material grains, confirming previous observations by TEM analysis. Semi-quantitative EDS

analysis showed an atomic distribution very similar to that recorded by XPS analysis (Table 1), consistent with a Sn surface concentration of approximately 8 at.% in the Sn-CaP sample. Moreover, only traces of chlorine were detected, confirming the almost complete removal of residuals derived from the $SnCl_2$ precursor (see Fig. S.3A).

3.4. Tin speciation by Mössbauer analysis

To investigate the chemical speciation of tin in Sn-CaP, Mössbauer spectra of samples stored under nitrogen or air were acquired. Mössbauer spectroscopy provides a particular tool for distinguishing Sn(II) and Sn(IV) components since their characteristic isomer shift (δ) and quadrupole splitting (Δ) values are distinctly different.

The spectra shown in Fig. 5 and parameters collected in Table 2 are consistent with results from other studies on similar tin phosphates, although some scatter can be observed. Specifically, Sn(IV) isomer shift (δ) data are generally close to 0.0 mm s^{-1} for all samples (Table 2), while Sn(II) isomer shift (δ) values are slightly smaller than those reported for Sn(II)-containing phosphate glasses prepared from melts of component salts at 450-1000 °C (~ 3.1 mm s^{-1}) [48,49]. Even larger Sn(II) isomer shift values were observed for certain tin phosphates prepared in aqueous media (~ 3.6 mm s^{-1}) [50], whereas NH_4^+-Sn(II) phosphites exhibit similar isomer shift values as shown in Table 2 with slightly smaller quadrupole splitting (Δ) values [51]. Certain tin amorphous composite oxides ($SnB_{0.6}P_{0.4}O_{2.9}$) exhibit similar parameters as reported in Table 2 [52].

In addition, the presented Sn(II) parameters in Table 2 can be discussed in comparison with hydroxostannate compounds. In particular, di- and trinuclear Sn(II) hydroxostannates exhibit similar δ and Δ values depending on the oxide/hydroxide relative distribution within them [53]. Thus, the presence of hydroromarchite in Sn-CaP, revealed by XRPD analysis, seems to agree with Mössbauer data as well. However, the XRPD diffractogram exhibits a large amorphous background (Fig. 2), and the amorphous part could probably be attributed to phosphates or mixed hydroxophosphates.

Table 2. Mössbauer parameters of Sn-CaP samples acquired at room temperature and at -193 °C.

	Temperature	**RT**						**~ -193 °C**					
	Component	**Sn(IV)**			**Sn(II)**			**Sn(IV)**			**Sn(II)**		
	Parameter	**δ** [a]	**Δ** [b]	**Rel. Int.** [c]	**δ**	**Δ**	**Rel. Int.**	**Δ**	**Δ**	**Rel. Int.**	**δ**	**Δ**	**Rel. Int.**
I	Fresh / air	0.01	0.61	69.4	2.95	2.06	30.6	0.05	0.62	53.3	2.93	2.05	46.7
II	Aged (180 days)	0.02	0.66	100	- [f]	-	-	n.a.[g]	n.a.	n.a.	n.a.	n.a.	n.a.
III	Calcined (550 °C for 1 h)	-0.05 0.32 [d]	0.70 0.84 [d]	63.7 36.3 [d]	-	-	-	n.a.	n.a.	n.a.	n.a.	n.a.	n.a.
IV	Used (with Cr) [e]	0.00	0.71	87.6	2.99	1.92	12.4	0.03	0.75	77.2	2.93	2.03	22.8

[a] isomer shift (calibrated against a spectrum of a combined SnO_2 and β-Sn absorber at room temperature)

[b] quadrupole doublet

[c] relative spectral area

[d] spectrum fitted with two Sn(IV) doublets (the second doublet may probably be assigned to another Sn(IV) compound)

[e] sample after use in the reductive adsorption of Cr(VI)

[f] not detected

[g] not analyzed

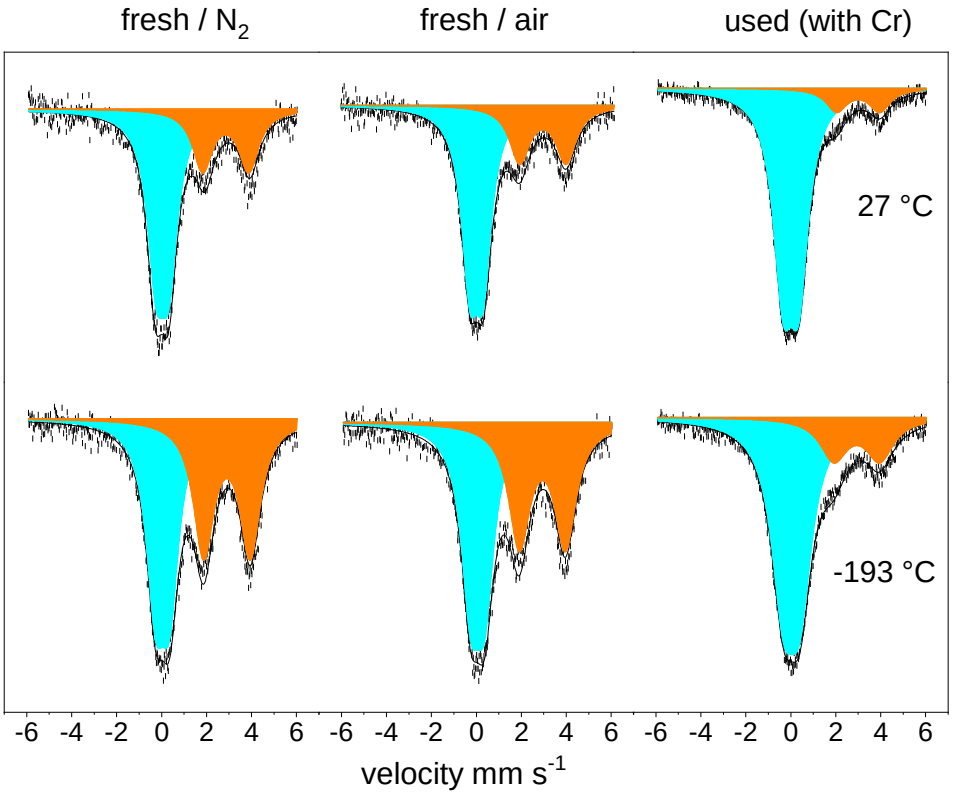

Figure 5. Mössbauer spectra of Sn-CaP samples displaying simultaneous presence of Sn(II) (orange) and Sn(IV) (cyan) contributions on both measuring temperatures (27 °C, top and -193 °C, bottom).

For a more quantitative estimation of the amount of Sn(II) and Sn(IV) components, the probability of the Mössbauer effect (the so-called f-factor) depends significantly on temperature and merits investigation. Namely, this dependence is more pronounced for Sn(II) than for Sn(IV) [54]. First, the values of corresponding Debye temperatures (Θ_D) can be estimated by comparing the relative contributions of Sn(II) and Sn(IV) in the spectra collected at -193 °C and 27 °C [55]. In the next step, the related f-factors can be calculated and used to estimate the actual amount of Sn(II) and Sn(IV). A more detailed description of this calculation is reported in paragraph S.4 of ESI. The obtained values are presented in Table 3.

The estimated amount of Sn(II) and Sn(IV) reported in Table 3 for Sn-CaP revealed Sn(II) species as the major component of the sample (approximately 55%), which seems to contrast with the results obtained from XRPD analysis. According to the Rietveld refinement, the weight fraction of the $Sn_6O_4(OH)_4$ phase (containing Sn(II) species) is only ≈34%, while the SnO_2 phase is ≈66%. This apparent discrepancy in the Sn(II)/Sn(IV) distribution could be attributed to the amorphous phase of Ca-phosphate also present in the sample, which cannot be estimated by the Rietveld refinement.

Indeed, considering that a partial Ca(II)/Sn(II) ion substitution can occur in the phosphate matrix, an increase in the Sn(II) amount would be observed in that case.

In summary, the primary result of the Mössbauer analysis is the clear (close to quantitative) distinction between Sn(II) and Sn(IV) components, whereas their coordinative environment (phosphate vs. (hydr)oxo) is far to be identified.

Table 3. Estimated amount of Sn(II) and Sn(IV) components in Sn-CaP samples as determined from Mössbauer spectra.

Sample	Component	Θ_D [a]	$f_{(-193\ °C)}$ [b]	Estimated proportions
Fresh/air	Sn(IV)	-61	0.728	0.45
	Sn(II)	-118	0.554	0.55
Used (with Cr)	Sn(IV)	-12	0.810	0.72
	Sn(II)	-100	0.619	0.28

[a] Debye temperature (°C), [b] f-factor (connected to probability of Mössbauer effect)

3.5. Hexavalent chromium reductive adsorption

The presence of Sn(II) in the hydroromarchite phase as well as in the amorphous calcium phosphate could impart reductive activity towards Cr(VI), as already demonstrated for Sn(II)-hydroxyapatite material [29]. Therefore, the performance of Sn-CaP in the reductive adsorption of Cr(VI) was assessed under the same conditions previously validated for Sn(II)-hydroxyapatite ([Cr(VI)]° = 100 mg L^{-1}; pH = 2; T = 25 °C; dosage of 4.5 g L^{-1}) [29,39]. Under the selected conditions, Sn-CaP exhibited a good removal capability for Cr(VI) (16.3 mg g^{-1}), a performance comparable to the Cr(VI) removal capacity of Sn(II)-hydroxyapatite (19 mg g^{-1}) [29].

The impact of pH on the reductive adsorption of Cr(VI) by Sn-CaP was systematically studied in a pH range from 2 to 11. Results obtained in terms of removal efficiency (η) and removal capacity (q_e) of Cr(VI) are reported in Fig. 6 and Table S.4. Sn-CaP exhibited high reductive activity throughout the entire pH range studied, with the highest activity observed under highly acidic (pH 2) and strongly basic (pH 11) conditions, being able to remove up to 16.3 and 15.5 mg_{Cr} g^{-1}, respectively.

The different pH conditions could induce different mechanisms by which the Cr(VI) reductive adsorption process occurs. Indeed, pH has well-established effects on the speciation of Cr(VI) compounds and also on surface properties of Sn-CaP, influencing the surface charge distribution. The measured value of the Sn-CaP point of zero charge (PZC) was found to be 7.4; then, lower and higher pH values than PZC gave rise to positively and negatively charged surfaces, respectively. At pH 2, the main Cr(VI) species are $Cr_2O_7^{2-}$ and $HCrO_4^-$, and an attractive electrostatic interaction may occur

with the positively charged surface of Sn-CaP, leading to a favourable adsorption process. Conversely, the CrO_4^{2-} species starts to become predominant at pH 11. At this pH value, the interaction with the negatively charged surface might be unfavourable for the CrO_4^{2-} adsorption. However, electron transfer between Cr(VI) and Sn(II) could be facilitated by an excess of OH^- presence. These different physical and chemical phenomena involved in the interaction between the various Cr(VI) species and Sn-CaP surface could be responsible for the variability of the observed results reported in Fig. 6 collected at pH values between 5 and 10.

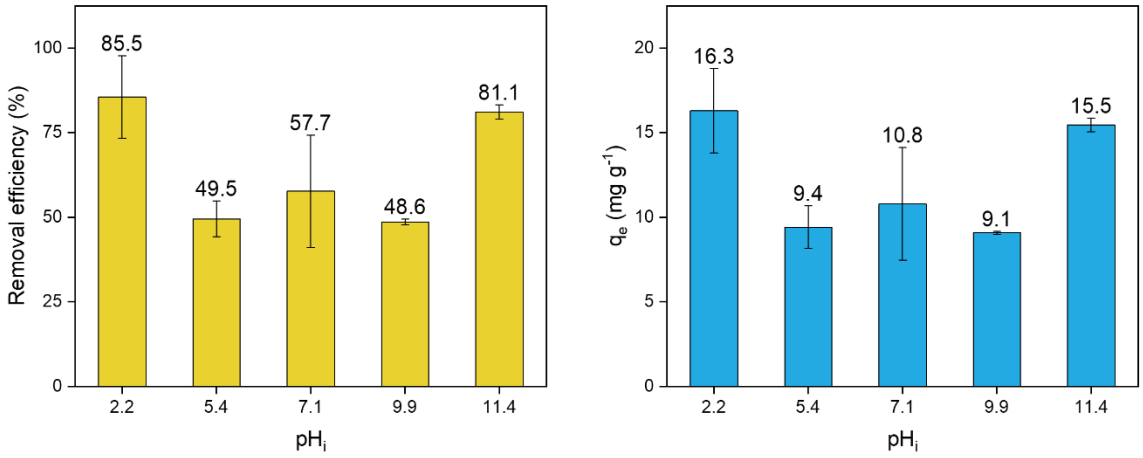

Figure 6. Effect of initial pH of Cr(VI) solution on the removal efficiency (η, yellow bars) and removal capacity (q_e, blue bars) of Cr(VI) by Sn-CaP ([Cr(VI)]° = 100 mg L^{-1}; T = 25 °C; dosage of 4.5 g L^{-1}).

The kinetics of Cr(VI) reductive adsorption onto the Sn-CaP sample was investigated at 25 °C in the co-presence of other cations, such as Fe(III), Co(II), Ni(II), Ca(II), Mg(II), and anions, such as chloride, nitrate, and sulphate, frequently found in Cr(VI) contaminated waters [41].

The experimental profiles of residual Cr(VI) concentration as a function of time are reported in Fig. 7. Pseudo-first order (PFO), pseudo-second order (PSO) and Elovich kinetic models have been used to fit all the experimental data, and the resulting kinetic parameters are reported in Table S.5 together with the corresponding statistical parameters. Both PSO and Elovich models are the best at fitting the experimental data, as demonstrated by the corresponding high R^2 and low Akaike Information Criterion (AIC) values (Table S.5).

A significant increase in the reaction rate was observed in the presence of cations; the calculated rate constant passed from 0.0058 g·mg^{-1}·min^{-1} to 0.0147 g·mg^{-1}·min^{-1}, in absence and presence of cations, respectively. This observation, already reported in the literature for other reductive adsorbents [39,56], has been associated with an easier diffusion of Cr(VI) ions within the electric double layer surrounding the adsorbent surface [39,40].

Interestingly, the Sn-CaP sample was also able to uptake the co-cations (Fe(III), Co(II), Ni(II)) from aqueous solutions without limiting Cr(VI) adsorption.

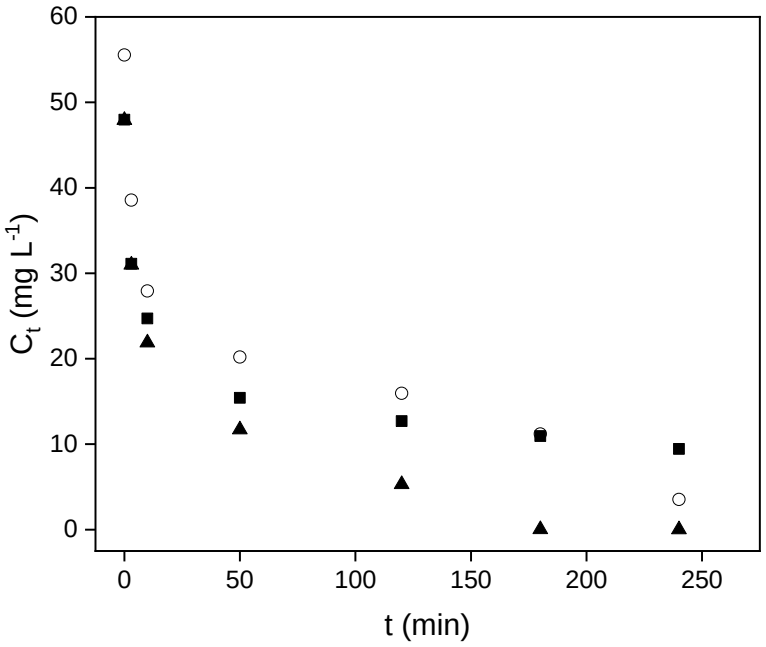

Figure 7. Kinetics of Cr(VI) reductive adsorption in water (empty circles), in the presence of cations (square markers, [Fe(III)]°=[Co(II)]°=[Ni(II)]° = 80 μg L^{-1}, [Ca(II)]°=[Mg(II)]° = 200 mg L^{-1}, nitrate salts), and in the presence of anions (triangle markers, [Cl^-]°=[NO_3^-]°=[SO_4^{2-}]° = 400 mg L^{-1}, sodic salts). Reduction test conditions: [Cr(VI)]° = 50 mg L^{-1}; generated pH of 4.8-5.7; T = 25 °C; dosage of 4.5 g L^{-1}.

3.6. Sn-CaP stability

It is known that atmospheric oxygen can induce unavoidable oxidation of Sn(II) to Sn(IV), thus affecting the stability of Sn-CaP and its functionality in Cr(VI) reductive adsorption. Mössbauer analyses demonstrated that in the short term, the relative distributions of Sn(II) and Sn(IV) were not influenced by the atmosphere (see comparison between N_2-stored and air-stored Sn-CaP samples in Fig. 5). However, it is important to evaluate the stability of the oxidation state of Sn(II) after long-term exposure to the oxidative atmosphere.

Synthesized samples were stored in closed vessels containing air for up to approximately 10 months and tested for reductive adsorption of Cr(VI) at different time intervals after their preparation. The obtained results are detailed in Table 4 and depicted in Fig. 8. Sn-CaP maintained removal efficiencies higher than 85% during the initial two weeks post-preparation, with no significant decline in activity, in agreement with Mössbauer analysis (Fig. 5). After this period, an exponential decay in the reductive activity was observed over time, resulting in almost complete loss of activity after ca. 300 days from its preparation.

Table 4. Effect of aging time on the Cr(VI) reductive adsorption activity of Sn-CaP ([Cr(VI)]° = 100 mg L^{-1}; pH = 2.0; T = 25 °C; dosage of 4.5 g L^{-1}).

Aging time (day)	q_e ($mmol_{Cr}/g$)	Removal efficiency (%)	Activity loss (%) [a]
1-14	0.31 ± 0.05	86 ± 12	-
84-91	0.08 ± 0.03	21 ± 10	75
169	0.05	16	82
287	0.02	6	93

[a] Based on the maximum removal efficiency

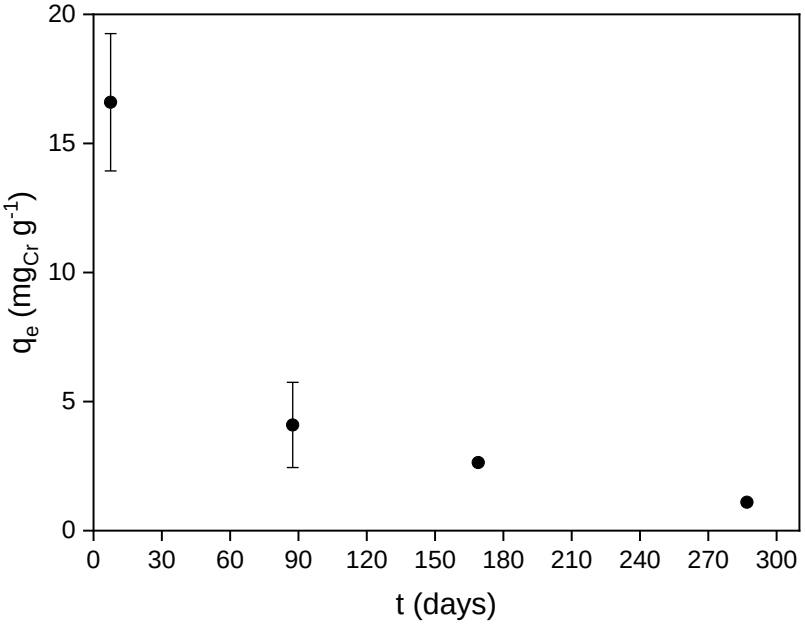

Figure 8. Cr(VI) removal capacity (q_e) as a function of aging time of Sn-CaP (reduction test conditions: [Cr(VI)]° = 100 mg L^{-1}; pH = 2.0; T = 25 °C; dosage of 4.5 g L^{-1}).

As evidenced in Table 2 and shown in Fig. S.4, the Mössbauer spectrum of an aged Sn-CaP sample, i.e., after 180 days from its preparation, exhibited the only contribution of Sn(IV), confirming the occurrence of the oxidation of Sn(II) over time. As expected, the newly formed Sn(IV) species were inactive in the Cr(VI) reductive adsorption process.

To address the decline in the Cr(VI) reductive activity of aged Sn-CaP, a chemical regeneration treatment was then explored.

Hydrogen temperature programmed reduction (H_2-TPR) analysis was performed to identify the optimal temperature to restore Sn(II) at the aged surface of Sn-CaP. The reduction profiles of the fresh and aged Sn-CaP samples are comparatively shown in Fig. S.5. Two main peaks characterized the reduction profiles of fresh and aged samples: a first reduction peak at around 350 °C, which can be

attributed to the reduction of Sn(IV) to Sn(II) [57], and a second prominent peak assigned to Sn(II) species being reduced to Sn(0) [57].

The total amount of H_2 consumed in each analysis is reported in Table S.6. It is worth noting that the aged sample consumed about 15% more H_2 than the fresh parent material. This increase could be attributed to a higher amount of Sn(IV) present in the aged sample because of the oxidation of Sn(II) over time, as already revealed by Mössbauer findings.

Based on H_2-TPR results, a hydrogenation treatment of aged Sn-CaP was carried out at 350 °C for 4 hours. The reduction profile resulting is shown in Fig. S.5, from which a partial restoration of Sn(II) presence could be inferred. Furthermore, the fresh and H_2-treated samples practically share the same H_2 consumption (Table S.6), which further hints at a restoration of the initial reducibility profile.

Then, a Cr(VI) reductive adsorption test was carried out using the H_2-treated sample to validate the efficient restoration of Sn(II) species. The regeneration treatment successfully recovered more than 50% of the reductive activity observed in the fresh sample.

3.7. Mechanism in hexavalent chromium removal

In-depth examination analysis was undertaken to discern whether the removal of Cr(VI) was solely attributed to a reductive adsorption mechanism or if other pathway, such as direct Cr(VI) adsorption, was implicated. Utilizing HAADF-STEM/EDS, XPS, and Mössbauer analyses, we investigated used Sn-CaP samples to elucidate the reaction mechanism.

The HAADF-STEM/EDS elemental mapping of the Sn-CaP sample (Fig. S.6) revealed a homogeneous dispersion of chromium across the examined grains, as indicated in the green-colored panel of Fig. S.6.

XPS analysis was carried out on Sn-CaP to elucidate the speciation of adsorbed chromium. The results, as presented in Table 5, showed a chromium content of 1.8 at.% at the surface.

Table 5. Surface composition of used Sn-CaP.

XPS (at.%)	**Cr**	**Sn**	**Ca**	**P**	**O**
Used (with Cr) [a]	1.8	7.2	8.1	12.1	70.9
Calcined (with Cr) [b]	2.0	8.8	12.1	14.9	62.2

[a] $[Cr(VI)]° = 100$ mg L^{-1}; pH = 2.0; T = 25 °C; dosage of 4.5 g L^{-1}
[b] 550 °C for 1 h

Further insight into chromium speciation was gained through a high-resolution spectrum in the Cr 2p region, depicted in Fig. 9. The spectrum displayed two main peaks corresponding to the $2p_{3/2}$ and $2p_{1/2}$ core levels of chromium, with binding energy (BE) values of approximatively 577 and 588 eV, respectively. Deconvolution of the spectrum into sub-bands revealed the sole presence of Cr(III) in a

typical hydroxide environment (bands centered at 577.4 eV and 586.6 eV with spin-orbit splitting of 9.3 eV) [58]. From the XPS results, it can be inferred that the mechanism underlying Cr(VI) removal likely entails an exclusive reductive adsorption.

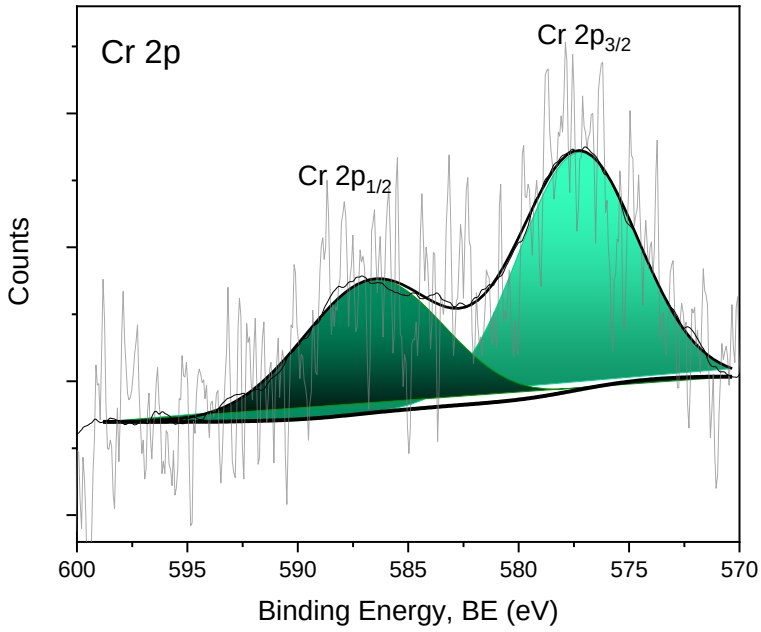

Figure 9. High-resolution XPS spectrum of Cr 2p region for Sn-CaP after its use in the reductive adsorption of Cr(VI).

Mössbauer spectra of the Sn-CaP sample after use revealed that the Sn(II) component in the main peak was less pronounced than that of the sample before use (Fig. 5). The parameters reported in Table 3 showed that the relative contribution of Sn(IV) increased from 45% to 72%, confirming that the reductive process of Cr(VI) to Cr(III) proceeded at the expense of Sn(II) that was oxidized to Sn(IV).

Based on the XRPD and Mössbauer results discussed above, the reduction of Cr(VI) to Cr(III) could potentially occur either on the hydroromarchite phase ($Sn_6O_4(OH)_4$) [59,60] or on Sn(II) dispersed at the surface of the calcium phosphate phase. Pinakidou *et al.* [59] demonstrated the occurrence of transformation of $Sn_6O_4(OH)_4$ to SnO_2 after the reduction of Cr(VI) to Cr(III) and proposed that the adsorption of Cr(III) took place directly onto the formed SnO_2 through the formation of inner sphere complexes. Indeed, the adsorption of Cr(III) onto $Sn_6O_4(OH)_4$ is not feasible due to the geometrical structure of $Sn_6O_4(OH)_4$, which is incompatible with the adsorption of Cr(III). In our case, considering that the SnO_2 phase is already present in the pristine Sn-CaP sample, it can be inferred that the adsorption of Cr(III) occurred on both the pristine and freshly formed SnO_2 phases.

Residual concentrations of both total and hexavalent chromium were determined at the end of each test of Cr(VI) removal to calculate Cr(III) concentration in solution. Since Cr(III) was not found in solution, it can be deduced that the complete adsorption of Cr(III) ions successful occurred.

Furthermore, following digestion of Sn-CaP after use, ICP-MS yielded a chromium amount comparable to that calculated as the difference between initial and residual total chromium concentrations. This finding seems to validate the proposed mechanism, which involves reductive adsorption, resulting in the quantitative adsorption of formed Cr(III) ions on the Sn-CaP surface.

3.8. Used Sn-CaP upcycling into a catalyst for NO oxidation

In the framework of a circular economy, embracing a waste valorization approach becomes essential to granting spent/used materials a second life. Given that both tin and chromium metal species are commonly utilized in oxidation catalysts, there is potential to design an upcycling *adsorbent-to-catalyst* strategy for the valorization of used Sn-CaP.

The selective catalytic oxidation of NO to NO_2 (equation 1) was chosen to evaluate the effectiveness of this approach.

$$NO + {}^{1}/_{2}\, O_2 \rightleftharpoons NO_2 \qquad (1)$$

This reaction plays a pivotal role in both industrial catalysis, such as the Ostwald process for nitric acid production, and environmental catalysis, serving as a critical step in various applications. These include: NO_x storage-reduction (NSR), where NO is oxidized to NO_2 and then stored as nitrates or nitrites before being reduced; continuously regenerating trap (CRT), where NO is converted to NO_2, which then oxidizes the soot collected on a diesel particulate filter; and selective catalytic reduction (SCR) of NO_x, where the "fast" SCR reaction involving NO, NH_3, and NO_2 is approximately 10 times faster than the standard reaction between only NO and NH_3. The reaction is spontaneous over a wide temperature range but is constrained by an equilibrium (K_{25}=1.17 10^6). According to Le Chatelier's principle, low temperature and high pressure values thermodynamically promote the formation of NO_2. To maximize the production of NO_2, it is necessary to design catalysts capable of expediting the attainment of equilibrium composition at the lowest feasible temperatures.

After the Cr(VI) reductive adsorption, used Sn-CaP sample, encompassing at its surface both Sn(IV) and Cr(III), underwent testing as a catalyst in the oxidation of nitric oxide to dinitrogen oxide, after calcination at 550 °C. The thermal treatment did not significantly alter the surface composition of the material, as indicated by XPS analysis (Table 5).

The catalytic performance of used Sn-CaP in NO oxidation reaction was assessed as a function of the temperature in comparison to that of the pristine Sn-CaP. Profiles of concentration of the formed NO_2 for both fresh and used Sn-CaP samples are reported in Fig. S.7. Sn-CaP was not active in the NO oxidation at all temperatures, while the used Sn-CaP showed an interesting activity. The onset of catalytic activity of used Sn-CaP occurred at 250 °C, and NO conversion reached the equilibrium curve at 425 °C corresponding to the maximum conversion attainable.

Given the different catalysts and experimental conditions employed in literature for the NO oxidation reaction, comparing the catalytic performance of the Sn-CaP sample with others reported is a nontrivial task. To facilitate comparison, the catalytic activity was investigated across various gas hourly space velocity (GHSV) values (ranging from 15,000 to 80,000 h^{-1}) under selected isothermal conditions (350 °C); conversion of NO to NO_2 was calculated and normalized to the equilibrium conversion. In Fig. 10 the normalized conversion of NO to NO_2 is reported as a function of both temperature (at fixed GHSV of 50,000 h^{-1}) and GHSV (at fixed temperature of 350 °C). As expected, the NO conversion to NO_2 rose with temperature and with decreasing GHSV, reaching a maximum conversion of 93% at the lowest GHSV value of 15,000 h^{-1} and at 350 °C. Interestingly, within 15,000 and 30,000 h^{-1} of GHSV, the performance of the used Sn-CaP was comparable to that reported for various Mn-, Co-, Cr-, Ce-oxides, and/or mixed metal oxides [61]. A significant comparison arises with the Cr-based catalyst (CrO_x/TiO_2) proposed by Meng *et al.* [62], achieving a NO conversion of 50% at 350 °C (27,000 h^{-1}, 400 ppm NO, 10% O_2). Under similar conditions, used Sn-CaP achieved a NO conversion of 59% at the same temperature. This outcome highlights the validity of the proposed approach, as a catalyst derived from a spent/used adsorbent (used Sn-CaP) demonstrates performance matching that of a Cr-based catalyst (CrO_x/TiO_2) resulting from an optimization study of catalyst design.

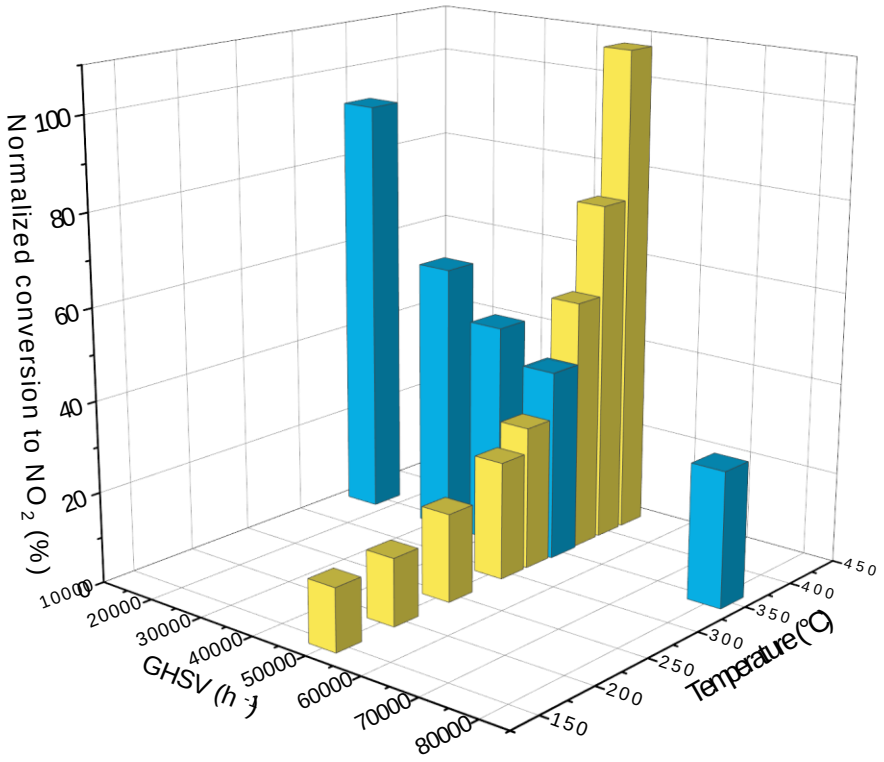

.

Figure 10. Effect of temperature (yellow bars, GHSV = 50,000 h^{-1}) and GHSV (blue bars, T = 350 °C) on the catalytic activity of used Sn-CaP in the oxidation of NO to NO_2 (NO = 800 ppm, O_2 = 40,000 ppm). Conversion of NO was normalized based on equilibrium curve calculated in the temperature interval 100-500 °C.

4. Conclusions

In summary, the synthesis of the Sn-CaP material here proposed through a sustainable one-pot co-precipitation method represents a significant advancement in environmental science, leading to a multifunctional material for water and air quality remediation.

An in-depth characterization study through XRPD and Mössbauer techniques unveiled a complex combination of crystalline phases, including cassiterite SnO_2 and hydroromarchite $Sn_6O_4(OH)_4$, along with an amorphous $Ca_3(PO_4)_2$ phase and provided insights into the speciation of Sn species. Notably, the presence of Sn(II) species on the surface provided remarkable efficacy to the Sn-CaP sample in the removal of Cr(VI). Demonstrating notable potential, the Sn-CaP sample acted as an effective functional material in the reductive adsorption of Cr(VI) across a wide pH range and in the presence of diverse contaminant cations.

The speciation of adsorbed chromium onto the Sn-CaP, determined through high-resolution XPS analysis, revealed a mechanism involving a sequential process of Cr(VI) reduction followed by Cr(III) adsorption onto the surface, defining reductive adsorption as the operative mechanism.

Finally, the Sn-CaP sample used for Cr(VI) removal, showed catalytic activity in the oxidation of NO to NO_2. This can be attributed to the oxidative properties of the Sn(IV) and Cr(III) species present on the surface, thus presenting an example of valorization of a used/exhausted material in a circular economy framework.

This multifunctional capacity of the calcium tin phosphate material highlights its potential to address environmental remediation challenges and contribute to the sustainable use of resources.

Acknowledgement

This work received financial support from the Università degli Studi di Milano (PSR2022_DIP_005_PI_RCONT and PSR2021_DIP_005_PI_SPIER projects "Piano di Sostegno alla Ricerca 2022, Linea 2, Azione A). Part of this project has been funded through the REACT EU resources by the NOP Research and Innovation 2014–2020.

Dr. Silvia Arici from A2A Ciclo Idrico, Brescia, Italy is gratefully acknowledged by all the authors for the analytical support.

All the authors are thankful to Dr. Zsolt Kasztovszky from Laboratory of Nuclear Analysis (NAL, Centre for Energy Studies, Budapest, Hungary) for the PGAA measurements and evaluation of γ radiation profiles.

The authors acknowledge the European Synchrotron Radiation Facility (ESRF, Grenoble) for provision of synchrotron radiation facilities and they would like to thank Dr. Stefano Checchia (beamline ID15A of the ESRF) for assistance and support in using beamline ID15A.

References

[1] J. Chen, Y. Qiu, X. Liu, L. Guo, Phenyl-modified carbon nitride based multifunctional gel for the detection, adsorption, photocatalytic reduction and recycling of chromium(VI) in wastewater, Appl. Surf. Sci. 652 (2024) 159278. https://doi.org/10.1016/j.apsusc.2023.159278.

[2] H. Jia, X. Zhang, X. Zeng, R. Cai, Z. Wang, Y. Yuan, T. Yue, Construction of silver nanoparticles anchored flower-like magnetic Fe3O4@SiO2@MnO2 hybrids with antibacterial and wound healing activity, Appl. Surf. Sci. 567 (2021) 150797. https://doi.org/10.1016/j.apsusc.2021.150797.

[3] C. Wang, Z. Su, L. Chen, H. Zhang, W. Hui, D. Liang, G. Zheng, L. Zhang, Z. Tang, W. Wen, J. Tang, Q. Huang, F. Song, Q. Chen, X. Gao, MoO3 doped PTAA for high-performance inverted perovskite solar cells, Appl. Surf. Sci. 571 (2022) 151301. https://doi.org/10.1016/j.apsusc.2021.151301.

[4] S. Sheng, Y. Song, L. Sha, K. Ye, K. Zhu, Y. Gao, J. Yan, G. Wang, D. Cao, Simultaneous hydrogen evolution and ethanol oxidation in alkaline medium via a self-supported bifunctional electrocatalyst of Ni-Fe phosphide/Ni foam, Appl. Surf. Sci. 561 (2021) 150080. https://doi.org/10.1016/j.apsusc.2021.150080.

[5] M. Guo, X. Min, J. Gu, K. Li, Z. Cheng, Z. Shen, J. Jia, T. Sun, In situ construction of Mn-Fe multi oxides derived from K2FeO4 and MnSO4 for high-efficient degradation of toluene, Appl. Surf. Sci. 644 (2024) 158687. https://doi.org/10.1016/j.apsusc.2023.158687.

[6] P. Sun, Y. Peng, M. Liu, J.-Y. Tian, S. Zhang, M. Wang, H. Zhu, C. Nie, Z. Zhang, M. Du, A novel MOF-based hollow carbon nanofiber mat with hierarchical apertures for efficient adsorption of low concentration benzene under high humidity, Appl. Surf. Sci. 644 (2024) 158761. https://doi.org/10.1016/j.apsusc.2023.158761.

[7] W. Huang, J. Xu, D. Lu, J. Deng, G. Shi, T. Zhou, Rational design of magnetic infinite coordination polymer core-shell nanoparticles as recyclable adsorbents for selective removal of anionic dyes from colored wastewater, Appl. Surf. Sci. 462 (2018) 453–465. https://doi.org/10.1016/j.apsusc.2018.08.122.

[8] K. Kumar, R. Kumar, S. Kaushal, N. Thakur, A. Umar, S. Akbar, A.A. Ibrahim, S. Baskoutas, Biomass waste-derived carbon materials for sustainable remediation of polluted environment: A comprehensive review, Chemosphere 345 (2023) 140419. https://doi.org/10.1016/j.chemosphere.2023.140419.

[9] T. Velempini, Meh. Ahamed, K. Pillay, Heavy-metal spent adsorbents reuse in catalytic, energy and forensic applications- a new approach in reducing secondary pollution associated with adsorption, Results Chem. 5 (2023) 100901. https://doi.org/10.1016/j.rechem.2023.100901.

[10] O. Peiravi-Rivash, M. Mashreghi, O. Baigenzhenov, A. Hosseini-Bandegharaei, Producing bacterial nano-cellulose and keratin from wastes to synthesize keratin/cellulose nanobiocomposite for removal of dyes and heavy metal ions from waters and wastewaters, Colloids Surf. A: Physicochem. Eng. Asp. 656 (2023) 130355. https://doi.org/10.1016/j.colsurfa.2022.130355.

[11] F.-F. Chen, Y. Liang, L. Chen, X. Liang, Y.-N. Feng, J. Wu, Y.-J. Zhu, Y. Yu, Upcycling of heavy metal adsorbents into sulfide semiconductors for photocatalytic CO2 reduction, Appl. Surf. Sci. 558 (2021) 149647. https://doi.org/10.1016/j.apsusc.2021.149647.

[12] R.S. Varma, Biomass-Derived Renewable Carbonaceous Materials for Sustainable Chemical and Environmental Applications, ACS Sustain. Chem. Eng. 7 (2019) 6458–6470. https://doi.org/10.1021/acssuschemeng.8b06550.

[13] R. Murugavel, A. Choudhury, M.G. Walawalkar, R. Pothiraja, C.N.R. Rao, Metal Complexes of Organophosphate Esters and Open-Framework Metal Phosphates: Synthesis, Structure, Transformations, and Applications, Chem. Rev. 108 (2008) 3549–3655. https://doi.org/10.1021/cr000119q.

[14] X. Li, A.M. Elshahawy, C. Guan, J. Wang, Metal Phosphides and Phosphates-based Electrodes for Electrochemical Supercapacitors, Small 13 (2017) 1701530. https://doi.org/10.1002/smll.201701530.

[15] A. Bouddouch, E. Amaterz, B. Bakiz, A. Taoufyq, F. Guinneton, S. Villain, J. Gavarri, M. Ezahri, J. Valmalette, A. Benlhachemi, Role of thermal decomposition process in the photocatalytic or photoluminescence properties of $BiPO_4$ polymorphs, Water Environ. Res. 92 (2020) 1874–1887. https://doi.org/10.1002/wer.1340.

[16] A. Bouddouch, E. Amaterz, A. Taoufyq, B. Bakiz, F. Guinneton, S. Villain, J.C. Valmalette, J.R. Gavarri, A. Benlhachemi, Photocatalytic and photoluminescent properties of a system based on SmPO4 nanostructure phase, Mater. Today: Proc. 27 (2020) 3139–3144. https://doi.org/10.1016/j.matpr.2020.03.803.

[17] N. Pan, J. Tang, D. Hou, H. Lei, D. Zhou, J. Ding, Enhanced uranium uptake from acidic media achieved on a novel iron phosphate adsorbent, Chem. Eng. J. 423 (2021) 130267. https://doi.org/10.1016/j.cej.2021.130267.

[18] H. Yaacoubi, O. Zidani, M. Mouflih, M. Gourai, S. Sebti, Removal of Cadmium from Water Using Natural Phosphate as Adsorbent, Procedia Eng. 83 (2014) 386–393. https://doi.org/10.1016/j.proeng.2014.09.039.

[19] J. Li, B. Li, W. Yu, H. Huang, J.-C. Han, Y. Huang, X. Wu, B. Young, G. Wang, Lanthanum-based adsorbents for phosphate reutilization: Interference factors, adsorbent regeneration, and research gaps, Sustainable Horizons 1 (2022) 100011. https://doi.org/10.1016/j.horiz.2022.100011.

[20] J. Xiong, Y. Dong Noh, W. Huang, S. Komarneni, Selectivity of transition metal ions by a layered tin phosphate, Mater. Lett. 309 (2022) 131450. https://doi.org/10.1016/j.matlet.2021.131450.

[21] J.A. Martens, P.A. Jacobs, Crystalline Microporous Phosphates: a Family of Versatile Catalysts and Adsorbents, in: Studies in Surface Science and Catalysis, Elsevier, 1994: pp. 653–685. https://doi.org/10.1016/S0167-2991(08)60781-8.

[22] H. Zhao, Z. Yuan, Insights into Transition Metal Phosphate Materials for Efficient Electrocatalysis, ChemCatChem 12 (2020) 3797–3810. https://doi.org/10.1002/cctc.202000360.

[23] C. Piccirillo, C.W. Dunnill, R.C. Pullar, D.M. Tobaldi, J.A. Labrincha, I.P. Parkin, M.M. Pintado, P.M.L. Castro, Calcium phosphate-based materials of natural origin showing photocatalytic activity, J. Mater. Chem. A 1 (2013) 6452. https://doi.org/10.1039/c3ta10673j.

[24] G. Garbarino, G. Pampararo, E. Finocchio, G. Busca, A. Gervasini, S. Campisi, B. Silvestri, C. Imparato, A. Aronne, Surface acid properties of Nb2O5–P2O5–SiO2 gel-derived catalysts, Microporous Mesoporous Mater. 343 (2022) 112190. https://doi.org/10.1016/j.micromeso.2022.112190.

[25] N.J. Clayden, C. Imparato, R. Avolio, G. Ferraro, M.E. Errico, A. Vergara, G. Busca, A. Gervasini, A. Aronne, B. Silvestri, Chloride-free hydrolytic sol–gel synthesis of Nb–P–Si oxides: an approach to solid acid materials, Green Chem. 22 (2020) 7140–7151. https://doi.org/10.1039/D0GC02519D.

[26] A. Gervasini, P. Carniti, F. Bossola, C. Imparato, P. Pernice, N.J. Clayden, A. Aronne, New Nb-P-Si ternary oxide materials and their use in heterogeneous acid catalysis, Mol. Catal. 458 (2018) 280–286. https://doi.org/10.1016/j.mcat.2017.10.006.

[27] M.N. Catrinck, S. Campisi, P. Carniti, R.F. Teófilo, F. Bossola, A. Gervasini, Phosphate Enrichment of Niobium-Based Catalytic Surfaces in Relation to Reactions of Carbohydrate Biomass Conversion: The Case Studies of Inulin Hydrolysis and Fructose Dehydration, Catalysts 11 (2021) 1077. https://doi.org/10.3390/catal11091077.

[28] S. Campisi, S. Bennici, A. Auroux, P. Carniti, A. Gervasini, A Rational Revisiting of Niobium Oxophosphate Catalysts for Carbohydrate Biomass Reactions, Top Catal 61 (2018) 1939–1948. https://doi.org/10.1007/s11244-018-0999-x.

[29] S. Campisi, M. Leone, M. Papacchini, C. Evangelisti, L. Polito, G. Postole, A. Gervasini, Multifunctional interfaces for multiple uses: Tin(II)-hydroxyapatite for reductive adsorption of Cr(VI) and its upcycling into catalyst for air protection reactions, J. Colloid Interface Sci. 630 (2023) 473–486. https://doi.org/10.1016/j.jcis.2022.10.116.

[30] Y. Yu, C. Du, Leaching of phosphorus from phosphate tailings and extraction of calcium phosphates: Toward comprehensive utilization of tailing resources, J. Environ. Manag. 347 (2023) 119159. https://doi.org/10.1016/j.jenvman.2023.119159.

[31] J.B. Duncan, K. Hagerty, W.P. Moore, R.N. Rhodes, J.M. Johnson, R.C. Moore, Laboratory Report On The Reduction And Stabilization (Immobilization) Of Pertechnetate To Technetium Dioxide Using Tin (II)apatite. LAB-RPT-12-00001, Rev. 0, Washington River Protection Solutions, Richland, WA., (2012).

[32] Z. Révay, Determining Elemental Composition Using Prompt γ Activation Analysis, Anal. Chem. 81 (2009) 6851–6859. https://doi.org/10.1021/ac9011705.

[33] L. Szentmiklósi, T. Belgya, Z. Révay, Z. Kis, Upgrade of the prompt gamma activation analysis and the neutron-induced prompt gamma spectroscopy facilities at the Budapest research reactor, J Radioanal Nucl Chem 286 (2010) 501–505. https://doi.org/10.1007/s10967-010-0765-4.

[34] Hyperlabs, https://www.hlabsoft.com, Hyperlabs, Https://Www.Hlabsoft.Com (2023).

[35] K. Kulcsár, D.L. Nagy, L. Pócs, A complete package of programs for the evaluation of Mössbauer and gamma spectra, KFKI Report 67 (1971).

[36] G.B.M. Vaughan, R. Baker, R. Barret, J. Bonnefoy, T. Buslaps, S. Checchia, D. Duran, F. Fihman, P. Got, J. Kieffer, S.A.J. Kimber, K. Martel, C. Morawe, D. Mottin, E. Papillon, S. Petitdemange, A. Vamvakeros, J.-P. Vieux, M. Di Michiel, ID15A at the ESRF – a beamline for high speed *operando* X-

ray diffraction, diffraction tomography and total scattering, J Synchrotron Rad 27 (2020) 515–528. https://doi.org/10.1107/S1600577519016813.

[37] A.P. Hammersley, S.O. Svensson, M. Hanfland, A.N. Fitch, D. Hausermann, Two-dimensional detector software: From real detector to idealised image or two-theta scan, High Press. Res. 14 (1996) 235–248. https://doi.org/10.1080/08957959608201408.

[38] G. Ashiotis, A. Deschildre, Z. Nawaz, J.P. Wright, D. Karkoulis, F.E. Picca, J. Kieffer, The fast azimuthal integration Python library: *pyFAI*, J Appl Crystallogr 48 (2015) 510–519. https://doi.org/10.1107/S1600576715004306.

[39] T. Avola, S. Campisi, L. Polito, S. Arici, L. Ferruti, A. Gervasini, Addressing the issue of surface mechanisms and competitive effects in Cr(VI) reductive-adsorption on tin-hydroxyapatite in the presence of co-ions, Sci Rep 13 (2023) 18913. https://doi.org/10.1038/s41598-023-44852-7.

[40] S. Campisi, C. Evangelisti, G. Postole, A. Gervasini, Combination of interfacial reduction of hexavalent chromium and trivalent chromium immobilization on tin-functionalized hydroxyapatite materials, Applied Surface Science 539 (2021) 148227. https://doi.org/10.1016/j.apsusc.2020.148227.

[41] K. Matern, H. Weigand, A. Singh, T. Mansfeldt, Environmental status of groundwater affected by chromite ore processing residue (COPR) dumpsites during pre-monsoon and monsoon seasons, Environ Sci Pollut Res 24 (2017) 3582–3592. https://doi.org/10.1007/s11356-016-8110-2.

[42] M.G. Galloni, S. Campisi, A. Gervasini, S. Morandi, M. Manzoli, How hydroxyapatite governs surface Cu(II) and Fe(III) structuring: Effects in the N2O decomposition under highly oxidant atmosphere, Appl. Catal. A: Gen. 655 (2023) 119101. https://doi.org/10.1016/j.apcata.2023.119101.

[43] R. Ramesh, R. Jagannathan, Optical Properties of Ce^{3+} in Self-Assembled Strontium Chloro(hydroxy)apatite Nanocrystals, J. Phys. Chem. B 104 (2000) 8351–8360. https://doi.org/10.1021/jp001117c.

[44] W.H. Baur, A.A. Khan, Rutile-type compounds. IV. SiO2, GeO2 and a comparison with other rutile-type structures, Acta Crystallogr B Struct Crystallogr Cryst Chem 27 (1971) 2133–2139. https://doi.org/10.1107/S0567740871005466.

[45] H. Reuter, D. Schröder, K. Peckskamp, M6O4(OH)4 of M = Sn, Pb: Single Crystal Growth and Crystal Structure Determinations Far Away from Routine, Crystals 13 (2023) 739. https://doi.org/10.3390/cryst13050739.

[46] N. Dubrovinskaia, M. Messingschlager, L. Dubrovinsky, Tin weathering experiment set by nature for 300 years: natural crystals of the anthropogenic mineral hydroromarchite from Creussen, Bavaria, Germany, Eur. J. Mineral. 34 (2022) 563–572. https://doi.org/10.5194/ejm-34-563-2022.

[47] M. Yashima, A. Sakai, T. Kamiyama, A. Hoshikawa, Crystal structure analysis of β-tricalcium phosphate Ca3(PO4)2 by neutron powder diffraction, J. Solid State Chem. 175 (2003) 272–277. https://doi.org/10.1016/S0022-4596(03)00279-2.

[48] E. Bekaert, L. Montagne, L. Delevoye, G. Palavit, A. Wattiaux, NMR and Mössbauer characterization of tin(II)–tin(IV)–sodium phosphate glasses, J. Non-Cryst. Solids 345–346 (2004) 70–74. https://doi.org/10.1016/j.jnoncrysol.2004.07.070.

[49] D. Ehrt, Effect of OH-content on thermal and chemical properties of SnOP2O5 glasses, J. Non-Cryst. Solids 354 (2008) 546–552. https://doi.org/10.1016/j.jnoncrysol.2007.07.092.

[50] L. Szirtes, Zs. Révai, J. Megyeri, E. Kuzmann, Investigations of tin (II/IV) phosphates prepared by various methods, Mössbauer study and X-ray diffraction characterization, Radiat. Phys. Chem. 78 (2009) 239–243. https://doi.org/10.1016/j.radphyschem.2009.01.006.

[51] C.G. Davies, J.D. Donaldson, W.B. Simpson, Phosphite complexes of tin(II), J. Chem. Soc., A (1969) 417. https://doi.org/10.1039/j19690000417.

[52] D.E. Conte, A. Aboulaich, F. Robert, J. Olivier-Fourcade, J.-C. Jumas, C. Jordy, P. Willmann, Snx[BPO4]1−x composites as negative electrodes for lithium ion cells: Comparison with amorphous SnB0.6P0.4O2.9 and effect of composition, J. Solid State Chem. 183 (2010) 65–75. https://doi.org/10.1016/j.jssc.2009.10.015.

[53] C.G. Davies, J.D. Donaldson, The Mössbauer effect in tin(II) compounds, Part III. The spectra of trihydroxostannates(II) and of basic tin(II) salts, J. Chem. Soc. (A) (1968) 946–948.

[54] D.J. Stewart, O. Knop, R.E. Meads, W.G. Parker, Pyrochlores. IX. Partially Oxidized $Sn_2Nb_2O_7$ and $Sn_2Ta_2O_7$: A Mössbauer Study of Sn(II,IV) Compounds, Can. J. Chem. 51 (1973) 1041–1049. https://doi.org/10.1139/v73-154.

[55] A. Lengyel, Z. Klencsár, Z. Homonnay, P. Sipos, É.G. Bajnóczi, I. Pálinkó, E. Kuzmann, Goldanskii–Karyagin effect on hyperalkaline tin(II)-hydroxide, J Radioanal Nucl Chem 307 (2016) 1195–1201. https://doi.org/10.1007/s10967-015-4410-0.

[56] X. Lv, Y. Hu, J. Tang, T. Sheng, G. Jiang, X. Xu, Effects of co-existing ions and natural organic matter on removal of chromium (VI) from aqueous solution by nanoscale zero valent iron (nZVI)-Fe3O4 nanocomposites, Chem. Eng. J. 218 (2013) 55–64. https://doi.org/10.1016/j.cej.2012.12.026.

[57] K. Zhang, H. Zhang, X. Feng, Y. Wang, G. Wang, X. Zhu, C. Li, Remarkable Support Effect on the Reactivity of Sn-Based Catalyst for Ethylbenzene Dehydrogenation, Catal Lett 153 (2023) 921–930. https://doi.org/10.1007/s10562-022-04027-x.

[58] M.C. Biesinger, C. Brown, J.R. Mycroft, R.D. Davidson, N.S. McIntyre, X-ray photoelectron spectroscopy studies of chromium compounds, Surface & Interface Analysis 36 (2004) 1550–1563. https://doi.org/10.1002/sia.1983.

[59] F. Pinakidou, E. Kaprara, M. Katsikini, E.C. Paloura, K. Simeonidis, M. Mitrakas, Sn(II) oxy-hydroxides as potential adsorbents for Cr(VI)-uptake from drinking water: An X-ray absorption study, Science of The Total Environment 551–552 (2016) 246–253. https://doi.org/10.1016/j.scitotenv.2016.01.208.

[60] E. Kaprara, N. Tziarou, K. Kalaitzidou, K. Simeonidis, L. Balcells, E.V. Pannunzio, A. Zouboulis, M. Mitrakas, The use of Sn(II) oxy-hydroxides for the effective removal of Cr(VI) from water: Optimization

of synthesis parameters, Sci. Total Environ. 605–606 (2017) 190–198. https://doi.org/10.1016/j.scitotenv.2017.06.199.

[61] Z. Hong, Z. Wang, X. Li, Catalytic oxidation of nitric oxide (NO) over different catalysts: an overview, Catal. Sci. Technol. 7 (2017) 3440–3452. https://doi.org/10.1039/C7CY00760D.

[62] F. Meng, S. Zhang, X. Li, Y. Zeng, Q. Zhong, CrO assembled at the oxygen vacancies on black-TiO2 for NO oxidation, Mol. Catal. 473 (2019) 110393. https://doi.org/10.1016/j.mcat.2019.110393.

Declaration of interests

☒The authors declare that they have no known competing financial interests or personal relationships that could have appeared to influence the work reported in this paper.

☐The authors declare the following financial interests/personal relationships which may be considered as potential competing interests: